Distributed Fibre Optic Sensing of Axially Loaded Bored Piles

Loizos Pelecanos[1], Kenichi Soga[2], Mohammed Z. E. B. Elshafie[3], Nicholas de Battista[4], Cedric Kechavarzi[5], Chang Ye Gue[6], Yue Ouyang[7], Hyung-Joon Seo[8]

[1] Lecturer in Geotechnical Engineering, Department of Architecture & Civil Engineering, University of Bath. Claverton Down, Bath, BA2 7AY, United Kingdom. Formerly: Research Associate, University of Cambridge, United Kingdom. Email: L.Pelecanos@bath.ac.uk. (Corresponding Author).

[2] Chancellor's Professor of Civil Engineering, Department of Civil & Environmental Engineering, University of California, Berkeley. 760 Davis Hall, 94720-1710, United States of America. Formerly: Professor, University of Cambridge, United Kingdom. Email: Soga@berkeley.edu

[3] Lecturer in Construction Engineering, Centre for Smart Infrastructure & Construction, Department of Engineering, University of Cambridge. Trumpington Street, Cambridge, CB2 1PZ, United Kingdom. Email: ME254@cam.ac.uk

[4] Research Associate, Centre for Smart Infrastructure & Construction, Department of Engineering, University of Cambridge. Trumpington Street, Cambridge, CB2 1PZ, United Kingdom. Email: N.Debattista@eng.cam.ac.uk

[5] Training & Knowledge Transfer Manager, Centre for Smart Infrastructure & Construction, Department of Engineering, University of Cambridge. Trumpington Street, Cambridge, CB2 1PZ, United Kingdom. Email: CK209@cam.ac.uk

[6] PhD Research Student, Centre for Smart Infrastructure & Construction, Department of Engineering, University of Cambridge. Trumpington Street, Cambridge, CB2 1PZ, United Kingdom. Email: CYG20@cam.ac.uk

[7] Project Manager, Cementation Skanska. Formerly: University of Cambridge, United Kingdom. Neelands House, Pipering Lane, Doncaster, DN5 9NB, United Kingdom. Email: Echo.Ouyang@skanska.co.uk

[8] Lecturer, Department of Civil Engineering, Xi'an Jiaotong – Liverpool University, Shaanxi Sheng, China, 710048, China. Formerly: Research Associate, University of Cambridge, United Kingdom. Email: Hyungjoon.Seo@xjtlu.edu.cn

Abstract

Instrumented pile tests are vital to establish the performance of a pile and validate the assumptions made during initial design. Conventional instrumentation includes vibrating wire strain gauges and extensometers to measure the change in strain or displacements within a pile. While these strain and displacement gauges are very accurate, they only provide strain/displacement readings at discrete locations at which they are installed. It is therefore common to interpolate between two consecutive points to obtain the values corresponding to the data gaps in between; in practice, these discrete instrumented points could be tens of meters apart, at depths corresponding to different soil layers, and hence simple interpolation between the measurement points remains questionable. The Brillouin Optical Time Domain Reflectometry fibre optic strain sensing system however is able to provide distributed strain sensing along the entire length of the cable, enabling the full strain profile to be measured during a maintained pile load test. The strain data can also be integrated to obtain the displacement profile. In this paper, three case studies are presented where the performance of three concrete bored piles in London is investigated using both conventional vibrating wire strain gauges and distributed fibre optic strain sensing during maintained pile load tests which enabled comparisons to be made between the two instrumentation systems. In addition, finite element analyses were conducted for the three piles and it was found that the ability to measure the full strain profiles for each pile is highly advantageous in understanding the performance of the pile and in detecting any abnormalities in the pile behaviour.

Keywords: piles, field monitoring, fibre optic sensors, load transfer, pile load test, finite element analysis, pile instrumentation

1. Introduction

The overall geotechnical capacity of a pile is derived from the skin friction and the base resistance. The design process begins with evaluating moderately conservative soil parameters based on site investigation test results. Depending on the type of soil, different equations and methods for pile capacity can be used. For example, for piles in clay the α-method and the method proposed by Meyerhof (1965) are commonly used (e.g. in the UK) to predict the ultimate skin friction and end bearing resistance respectively. Other methods adopt direct correlations based on in situ soil investigation (e.g. CPT, SPT) (Eslami & Fellenius 1997), LCPC (Bustamante & Gianeselli 1982), IC method (Jardine & Chow 1996). More complex and rigorous numerical methods can also be employed for complicated pile problems such as piled groups (Kraft, Ray & Kakaaki 1981; Poulos 1989; Randolph 2003) and piled raft (Poulos & Davis 1974; Kitiyodom & Matsumoto 2003) foundations. Nevertheless, all of these methods are used in the design stage and therefore they only provide an estimate of a pile's behaviour. As such, instrumented pile tests are recommended by standard codes of practice (e.g. clause 7.5 of Eurocode 7) to quantify the performance of a pile in order to validate the initial design assumptions.

General preliminary pile tests (McCabe & Lehane 2006) include a number of vibrating wire strain gauges (VWSG), either in pairs or threes at several levels within the pile, along with a measurement of pile head settlement measured from an independent reference beam by linear voltage distance transducers (LVDT). This instrumentation scheme offers very useful but discrete data points (Lehane et al. 1993). Data from appropriately monitored pile load tests can provide a means to assess the behaviour of the pile and develop pile behaviour models (Comodromos & Bareka 2009) such as load transfer curves (Ménard 1963; Butterfield & Banergee 1971; Kraft, Ray & Kakaaki 1981; Frank & Zhao 1982; Poulos 1989; Lee 1993; Klar et al. 2006; Abchir et al. 2015; Seo et al. 2017).

Recent advances in geotechnical instrumentation include fibre optic (FO) technology such as Fibre Bragg Gratings (FBG) (Kersey & Morey 1993; Lee et al. 2004; Liu & Zhang 2012; Doherty et al. 2015) and distributed Brillouin Optical Time-Domain Reflectometry (BOTDR) (Kurashima et al. 1993; Soga 2014; Pelecanos et al. 2017). The latter technology offers near spatially-continuous strain data along the entire length of the pile, which can be further processed to provide detailed information regarding the pile behaviour and integrity and load-transfer properties (Pelecanos & Soga 2017; de Battista et al. 2016). The BOTDR technique has been successfully used to monitor various soil-structure interaction problems (Acikgoz et al. 2016; Acikgoz et al. 2017), including piles (Klar et al. 2006; Ouyang et al. 2015; Pelecanos et al. 2016), shafts/retaining walls (Mohamad et al. 2011; Schwamb et al. 2014; Schwamb & Soga 2015), tunnel linings (Mohamad et al. 2010; Mohamad et al. 2012; Cheung et al. 2010; de Battista et al. 2015; Di Murro et al. 2016; Soga et al. 2017), tunnelling and other geotechnical process-induced surface settlements (Hauswirth et al. 2014; Klar, Dromy & Linker 2014; Linker & Klar 2015), concrete cracking (Goldfeld & Klar 2013), soil slopes etc.

In this paper the BOTDR distributed monitoring technology is briefly discussed and its application in a number of pile load test cases (both top-loaded using an external reference frame and bi-directionally loaded using an Osterberg-cell) in London is explored. The monitoring data from the distributed BOTDR and discrete VWSG technologies in the three case studies is analysed and compared to shed light on the relative merits of each approach (continuous and discrete) and highlight their necessity in future reliable pile load testing. Finally, numerical analyses were conducted for each of the three piles and the results are presented in this paper to enable a better understanding of pile behaviour under loading.

2. Distributed fibre optic monitoring

This section provides a brief description of the principles of BOTDR. However, the complete description of the method and the associated experimental approaches required for calibration are well beyond the scope of this paper and they are therefore not included, as they can be found elsewhere in great detail (Mohamad 2007; Iten 2011; Soga 2014; Soga et al. 2015). More information about the fundamentals of light propagation can be obtained from relevant literature in the area of photonics (Horiguchi et al. 1995) as this is out of scope of this paper. A detailed description of the theory of distributed FO strain sensing and its applications in civil and geotechnical infrastructure is given by Kechavarzi et al. (2016)

2.1. Principle of Brillouin Optical Time Domain Reflectometry

A fibre optic (FO) cable allows light waves from a FO analyser to travel along its entire length through total internal reflection, irrespective of the orientation of the cable itself. This allows a signal to be carried over very long distances, such as for broadband Internet. Backscattered signals are generated as the light wave passes through the optical fibre and presents itself as Rayleigh, Raman and Brillouin spectrum. Within the Brillouin backscatter, it is found that the peak frequency experiences a shift that is generally considered to be linearly proportional to applied strain. Using the measured time required for the backscattered signal to return to the analyser, the specific location at which this frequency shift is observed can be estimated accurately. Therefore, the entire fibre optic cable is essentially serving as a distributed strain sensor.

The FO analyser sends a light with of 1550 nm wavelength into an optical fibre and the generated Brillouin spectrum of the back-scattered light has 25-27 MHz bandwidth and around 11 GHz central peak frequency when no strain is applied on the fibre. The back-scattered Brillouin central frequency, v_b, is related to the input light according to Eq. 1 and this is provided directly from the FO analyser.

$$v_b = \frac{2 \cdot n_f \cdot v_a}{\lambda_l}$$

Eq. 1

where n_f is the fibre core refractive index, v_α is the acoustic velocity in the fibre and λ_l is the wave length of the input light.

Changes in temperature and/or strain induce a density change in the cable and therefore change in the acoustic velocity, v_α, of the light too. As the strain or temperature at a given location change, the frequency of the backscattered light is shifted by an amount which is approximately linearly proportional to the applied strain, $\Delta\varepsilon$, or temperature, ΔT, according to Eq. 2.

$$\Delta v_b = \Delta v_{b0} + M \cdot \Delta\varepsilon + N \cdot \Delta T$$

Eq. 2

Where, v_{b0} is the central Brillouin peak frequency at zero strain and at a given temperature, $\Delta\varepsilon$ is the applied strain, ΔT is the temperature change, and M, N are the coefficients for strain and temperature change respectively. For an incident wavelength of 1550nm, the Brillouin frequency shift can vary from 9GHz to 13GHz depending on the different fibre properties. Therefore knowledge about of this frequency difference can provide information about the applied strain and temperature changes at the location where the back-scattered light was generated. As the speed of light is constant, the location can be evaluated by measuring the time since the light was initially sent into the fibre. Back-scattered light is generated at every point along the entire length of the fibre and therefore by resolving both time and frequency a continuous strain profile along the fibre can be determined.

For the case studies presented in this paper, either the AQ8603 analyser manufactured by Yokogawa Electric Corporation, Japan, or the NeubreScope NBX-5000 analyser manufactured by Neubrex, Japan, are employed. These are able to provide a minimum readout resolution between 0.05m and 0.1m with a spatial resolution of 0.5 to 1.0m. Spatial resolution implies that it produces a weighted average strain reading over 0.5 or 1m at every 0.05m length of the cable (this is considered as “spatially-continuous” or “distributed” data). These settings can be changed depending on the time allocated for the specific test. Essentially the technology offers a large number of strain data (every 0.05m to 0.1m in this case) along a structure embedded with fibre optic cables.

In addition to the clear advantage of measuring a full strain profile, its simplicity lies in the fact that only a single cable is required for the entire system, enabling its use in small diameter piles and eliminating the time and effort for cable management, that would be required for conventional strain gauges. No electricity is required other than to power the analyser itself, which could be located much further away in a safe, and convenient location on the construction site, as light waves travel efficiently through the fibre optic cables. The result is an instrumentation system which can provide a full strain profile of the pile.

2.2. Fibre Optic Cables

Strain on an optical fibre can be generated from two sources, mechanical or thermal. Therefore, two types of optical fibre cables are installed and are shown in Figure 2: Fujikura 4-core single mode fibres reinforced ribbon cable for strain sensing (strain sensing cable) and Excel 4-core single mode fibres loose tube for temperature compensation (temperature cable). While they are both attached to the reinforcement cage, the fibre optic cores of the temperature cable sit in a gel which isolates any transfer of mechanical strains from the outer coating. Thus it is only subjected to thermal changes. These measurements are used to compensate the readings measured from the strain cables to provide an accurate reading of interest, the actual mechanical strain.

2.3. Installation of FO Instrumentation

Installation of FO cables is usually done on site, as described in Figure 3. Long pile foundations typically consist of a number of steel reinforcement cage segments and therefore the bottom steel cage is instrumented on the ground. The FO cables (shown in blue colour in Figure 3) are running along the entire length of the bottom segment on two opposite sides of the pile and a loop of some FO cable is made close to the bottom of the segment. The longitudinal cables are pre-strained (i.e. a tensile strain is applied) using cable clamps at the two ends of the steel cage. Once the borehole is dug, the bottom cage is inserted and while the other cages are spliced onto the bottom cage and the whole pile lowered down in the borehole, the remaining FO cable is attached to them. Finally, the two ends of the FO cable run from the top of the pile to the FO analyser.

With the pile loaded axially, it is assumed that the concrete pile will have negligible hoop strain across its cross section and therefore a 10m loop cable for both strain and temperature is prepared and secured at the end of the bottom reinforcement cage to serve as a zero-strain loop for referencing and compensation purposes.

For the ease of data interpretation, a pre-strain of about 1000-2000με is often introduced to the strain cable. Anchorage is provided on the bottom loop end by cable wire clamps before stretching the strain cable to the predetermined pre-strain. Strain cable is then secured with another set of cable wire clamps at the top of the reinforcement cage before supplementing the anchorage by either spot gluing with epoxy glue or using cable ties at approximately every 0.5-1.0m interval. Temperature cables are loosely secured next to the strain cables with cable ties as they are routed to the top of the cage. Figure 4 (a) and (b) show the installed FO cables and sister-bar VWSGs on a foundation pile.

Once the bottom cage has been instrumented, it is lowered into the borehole. The fibre optic cables are then unwound from the reels on each side of the borehole as the cage is lowered. Pre-straining is carried out for the strain cables for subsequent reinforcement cages as well without epoxy glue due to time constraints. Concrete is subsequently poured in the borehole and as the concrete cures the FO cables become securely embedded within the pile. Further details of FO cable installation in piles established at University of Cambridge can be found in (Klar et al. 2006; Soga 2014; Soga et al. 2015).

2.4. FO data analysis

As described earlier, applied strain causes a shift in the peak Brillouin frequency in the optical fibre. Therefore, by measuring the frequency difference, one can obtain the applied strain on the cable. Moreover, because FO cables are able to detect strains due to both mechanical and thermal loads, the two components need to be analysed separately. The measured frequency difference from the “temperature cable”, Δv_{bT}, is influenced only by changes in temperature, whereas that from the “strain cable”, Δv_{bS}, is influenced by changes in both mechanical load and temperature.

Therefore, changes in temperature, ΔT, can be obtained from Eq. 3 (where, C_{TT} is a property of the cable, obtained by calibrating the “temperature cable”, which determines how temperature affects the Brillouin frequency reading of the cable and it is usually around $1.1 \cdot 10^{-3}$ GHz/°C).

$$\Delta T = \frac{\Delta v_{bT}}{C_{TT}}$$

Eq. 3

The thermal strain, ε_{temp}, (the strain that corresponds to free thermal expansion strain due to temperature change) is then given by Eq. 4 (where, α_c is the thermal expansion coefficient of concrete and it is usually around 9.65 με/°C).

$$\varepsilon_{temp} = a_c \cdot \Delta T$$

Eq. 4

The real (observed) strain, ε_{real}, (the actual strain that the pile experiences in the field) is then given by Eq. 5 (where, C_E is a property of the fibre, obtained by calibrating the "strain cable", which determines how strain affects the Brillouin frequency and it is usually around $5 \cdot 10^{-4}$ GHz/με; and C_T is a property of the fibre that determines how the Brillouin frequency is affected by temperature difference, and it is usually around $1.0 \cdot 10^{-3}$ GHz/°C).

$$\varepsilon_{real} = \frac{1}{C_E}(\Delta v_{bS} - C_T \cdot \Delta T)$$

Eq. 5

The mechanical (constrained) strain, ε_{mech}, (the reaction strain that is the result of both the applied mechanical load and temperature) is then given by Eq. 6

$$\varepsilon_{mech} = \varepsilon_{real} - \varepsilon_{temp} = \frac{1}{C_E}\left[\Delta v_{bS} - C_T \cdot \left(\frac{\Delta v_{bT}}{C_{TT}}\right)\right] - a_c \cdot \frac{\Delta v_{bT}}{C_{TT}}$$

Eq. 6

Finally, once the strain profiles are obtained, the actual geotechnical response of the pile may be captured using Eq. 7 and Eq. 8 to determine axial force, $F_a(y)$, and vertical displacement, $u(y)$, profiles respectively.

$$F_a(y) = EA \cdot \varepsilon_{mech}(y)$$

Eq. 7

$$u(y) = u(y = y_0) + \int_0^y \varepsilon_{real}(y)\, dy$$

Eq. 8

Where, EA is the axial rigidity of the pile (E is Young's modulus and A is cross-sectional area) and y is the depth from the top of the pile. For the vertical displacements, the relative displacements obtained from the integration of axial strains is added to available absolute displacement values from displacement transducers at y_0. The data profiles obtained from BOTDR have usually a wavy nature and therefore they need to be filtered prior to data analysis. The data presented in this study have been filtered using a second order Savitzky-Golay (1964) filter with a 31-point frame.

3. Case study 1: Pile load test at Broadgate Road, London.

3.1. Description of pile test

The Broadgate Road project in London was designed to house a fourteen-storey office building with two basement levels. Due to tight space restrictions along one side of the project, a number of mini piles of 0.305m diameter were constructed in close proximity to support the superstructure. A high-strength steel reinforcing case was inserted in the ground after the drilling process. The pile tested is 0.305m diameter (0.343m at the top 6m because of a steel casing around the pile) and 25m long, as shown in Figure 5 (a). On the same figure, the soil stratigraphy is also included with some known material properties obtained from relevant triaxial and simple shear laboratory tests. The pile test was carried out once the concrete material achieved a specified value of minimum strength. The pile test consists of three consecutive cycles of applied load (at the top of the pile) of up to 720kN, 1080kN and 1985kN for each of the three cycles, achieved after several loading and unloading steps (Figure 5 (b)). The pile was instrumented with distributed FO cables on two opposite sides of the pile and a number of discrete VWSGs along the pile depth.

3.2. Data Interpretation

Figure 6(a) shows the axial strain in the pile for the three peak values of the three cycles as it was captured by the FO cables and the VWSGs, whereas Figure 6(b) shows the corresponding axial force profiles (calculated from strains multiplied by the pile axial rigidity, EA, as described by Eq. 7 and using E=30000MPa. This value adopted for E was obtained following the Fellenius (1989) approach and by using the FO strain values, ε, at the top 30cm of the pile (surrounded by soil but with insignificant influence, see Figure 6a, Figure 9a, Figure 12a) and the applied loads, P, ($E=\Delta P/\Delta\varepsilon/A$). The Fellenius method proposes a smooth linear (best-fit) reduction of secant modulus with axial strains. Therefore, a representative average value of E over the dominant experienced strains (~300-700με) was adopted based on that best-fit line. It is shown that there is a generally good agreement between the two monitoring technologies. No VWSG data were obtained for the largest cycle (i.e. for loading of 1985kN), as there was a malfunction of the VWSG instruments, and therefore only FO data is available for this load case. It is also shown that there is some scatter in the FO data values which is currently a known issue with distributed FO strain sensing systems. This is because the standard resolution of FO is constant and about 30-50με and therefore this becomes relatively less significant for larger applied loads (which imply larger induced strains). The waviness of FO strains may offer a challenge when differentiating strain data profiles to obtain shaft friction values, but their spatial continuity allows for a distributed sensing of localised strains, e.g. necking, fracture etc., whereas, such localised features would not be identified by discrete monitoring systems (such as VWSGs). Figure 6(c) shows the vertical displacements, u, of the pile from the FO cables. The values from the FOs were obtained by integrating the strain profiles and adding those to absolute displacement measurements from displacement transducers at the top of the pile, as described by Eq. 8.

The results of a simplified numerical finite element (FE) beam-spring model are included for comparison in Figure 6. The simplified FE analysis considered a single vertical pile loaded axially from the top modelled with linear beam elements and represented the surrounding soil with non-linear springs which is a practical approach as opposed to the more common way of modelling the soil with solid elements. All the beam elements and non-linear springs contribute to the global stiffness matrix and therefore the global FE equilibrium equations. Due to the nonlinear nature of the soil-spring the external load is applied incrementally and the equations are solved using an iterative Modified Newton-Raphson technique. A number of different soil layers, associated with constant soil spring properties along the depth of each layer, were considered based on the ground conditions, although they did not follow exactly the soil stratigraphy. This simplified FE analysis approach is explained in the

Appendix in more detail. The behaviour of the pile was back-analysed to derive the properties of the soil springs which are subsequently used in the FE analysis to calculate the axial strain and vertical displacement profiles. Namely, the optimum set of properties of the soil springs was obtained that was able to reproduce well the observed axial strain and vertical displacement profiles from the FO readings. The values of the model parameters was obtained through a simple optimisation algorithm (here the Levenberg-Marquardt scheme was used (Levenberg 1944; Marduardt 1963)), in which the changing variables were the set of the model parameters (i.e. in this case 20 parameters, 4 for each of the 4 layers and 1 for the pile base) and the objective function was the difference of the axial strains obtained from the numerical model and those observed from the FOs. It is shown here that a good match is obtained between the field data (from FO & VWSGs) and the FE back-calculations.

Figure 7 (a) shows the calculated shaft friction (SF) profiles for the three peak values of the three cycles, from the FE analysis. Since the FO data exhibit some (inherent) undulations, deriving SF values from the slope of the axial force might be cumbersome. Therefore, here a “synthetic” approach is followed, where a numerical model is established that reproduces accurately the monitored axial strain and vertical displacements from FOs (see Figure 6) and then SF profiles are obtained from the FE analysis of the model. This numerical analysis approach was followed here due to the inability to obtain SF values directly from the wavy FO strains. In fact, direct estimation of SF requires differentiation of axial strains which in the case of wavy strain profiles leads to unrealistically large fluctuations of SF values with the depth of the pile. It is shown here that generally larger SF values are obtained within the London Clay stratum (i.e. at $z<-4$m) as compared to the SF observed at the top soil layers (i.e. at $z>-4$m). However, it is shown that at the bottom of the pile, very small SF values are mobilised, perhaps due to the small strains experienced by the pile. Since a numerical optimisation procedure was followed to obtain the SF, the small values of strains experienced at the bottom of the pile compared to the usual variation of FO strain data leads to a large noise-to-signal-ratio and therefore the evaluation of SF (i.e. determination of the actual slope of the strain profiles) values may become cumbersome.

Furthermore, Figure 7 (b)(c) show the evolution of SF with the applied load, P, and the 'local' vertical displacement, u, at various depths (according to the local soil stratigraphy) along the pile and the pile base pressure, q_b. Figure 7 shows that SF is mobilised early in the test, whereas the pile base pressure is mobilised at later stages for higher loads. As expected the SF development curves show an initial stiffness that drops with the displacement, due to the plasticity of the soil close to the pile shaft. It is clearly observed that the first layer (0-6m), which is covered by the pile casing does not show significant development of strains and approximately reaches an ultimate value of SF of about 20kPa. Besides, although the three layers considered within the London Clay show variable SF development, it is accepted that the majority of the London Clay reaches SF of about 70-100kPa, whereas the bottom of the London Clay shows minimal development of SF. However, this could probably be due to the small layer thickness considered in the data analysis (FO data exist in layer 4 between y=19-22.5m). Nevertheless, in general, the evolution of shaft friction with the vertical displacements seems to reach (roughly) a plateau for displacements of about 0.01-0.03m which is slightly less than 10% of the pile diameter.

Finally, Figure 7 (d) shows the relevant design t-z and q-z curves following the API (2002) methodology (see Appendix B). Although there are some differences between the observed (Figure 7 (c)) and design (Figure 7 (d)) curves, in general they seem to agree quite well yielding comparable values of ultimate pile shaft and base resistance.

3.3. Remarks

A typical interpretation of the geotechnical data would consider Eq. 9 and Eq. 10 to calculate the ultimate shaft capacity, q_s, and Eq. 11 and Eq. 12 for the base capacity, q_b of the pile (Salgado 2008; Knappett & Craig 2012; Tomlinson & Woodward 2014).

$$q_{s(cohesive)} = \alpha \cdot S_u$$

Eq. 9

$$q_{s(non-cohesive)} = \beta \cdot \sigma'_{vo} = K_o \cdot \tan\delta \cdot \sigma'_{vo}$$

Eq. 10

$$q_{b(cohesive)} = N_c \cdot S_u$$

Eq. 11

$$q_{b(non-cohesive)} = N_q \cdot \sigma'_{vo}$$

Eq. 12

where, α (usually around 0.5 for London Clay (Tomlinson 1997)) is the empirical shaft coefficient, K_o is the earth pressure at rest, δ (usually around 0.75φ) (Stas & Kulhawy 1984) is the pile-soil interface friction angle and N_q (usually around 50 (Berezantzev, Khristoforov & Golubkov 1961; Knappett & Craig 2012)) and N_c (usually its value is taken as 9 (Kulhawy & Prakoso 1999)) are the base bearing capacity coefficients.

Using the above equations and the geotechnical data in Figure 5 one would obtain an ultimate value of shaft capacity of 8kPa for the first layer (using Eq. 10) and about 32-120kPa for the second layer (using Eq. 9). These values compare well with the calculated values from FO in Figure 7, which suggest around 20kPa for the first layer and about 10-120kPa for the second layer. If one was to back calculate the values of α and β, then, the first layer would yield a value of β=0.5 (whereas Eq. 10 yields β=0.2) and layers 2-4 would yield values of α=0.9, 0.89, 0.1 respectively (whereas the common assumption is 0.5 (Tomlinson 1997)).

Similarly, when calculating the ultimate base capacity, one would obtain about 2MPa when using Eq. 11 (i.e. based on S_u) and about 25MPa when using Eq. 12 (i.e. based on c and φ). These values are different and below and well above the (linear) 6MPa that was observed from the FOs during this test respectively. This is unexpected and it could be due to a number of possible reasons, e.g. it may suggest that the relation usually used for the pile base bearing capacity (Eq. 11) might be significantly unconservative or it may suggest that the material parameter values used to calculate σ'_{v0} were too small. Nevertheless, it is observed here that Eq. 11 (i.e. S_u) provides a better estimate.

The ability to fit a numerical model to the monitoring data (in particular, the continuous vertical displacement profile) to further understand the behaviour of piles is a great advantage. More confidence in the results of the back-analysed model is built when a continuous strain profile is available which can show the full picture of the strains over the whole length of the pile and by direct integration it may give reliable estimates of pile displacements. Finally, the benefits of obtaining such a relevant numerical model can include the development of load transfer curves derived from the calculated shaft friction with respect to the vertical displacement.

4. Case study 2: Pile load test at East Village, London.

4.1. Description of pile test

The second case study considers a pile test at East Village (former Athletes Village) in Stratford, London. The examined pile is 32m long with 900mm diameter (930mm at the top 14m). The local soil stratigraphy consists of Made Ground, Alluvium and River Terrace Deposit finishing at around 14m depth and along which the pile is covered by a 15mm-thick steel casing. These layers are followed by two thick layers of Lambeth Group and Thanet Sand that interface at a depth of 23m. Information about pile geometry, soil stratigraphy and some basic soil properties are given in Figure 8(a). The pile test consists of a static maintained load applied at the top of the pile following two cycles of loading-unloading until the pile fails. Details about the pile test sequence are shown in Figure 8(b). Similar to the previous case, the pile was instrumented with distributed FO cables and discrete VWSGs; the latter were installed at various locations along the pile depth.

4.2. Data Interpretation

Figure 9 (a)(b) show the monitored axial strains and the calculated axial force in the pile for three selected load stages from both the FOs and the VWSGs. Similar to the previous case, although the FOs show some scatter in the data, a good agreement is obtained between the two sensors for both strains and forces. Observed strains and forces are roughly constant for the first 14m which suggests that minor shaft friction is developed over that depth. This was expected as the pile is surrounded by a steel casing at the top 14m. Moreover, at depths below 14m, the axial strains and forces drop, which is due to the interaction with the surrounding soil and the developed soil-pile interface friction. Additionally, on the same graphs, the results of a simple FE analysis (similar to the one used in the first case, see Appendix A for more details and model parameters) are included (the strain step in the first figure is due to the change of pile diameter and hence the axial stiffness EA). This analysis was conducted to match the observed axial strains and vertical displacements in Figure 9 (a) and (c). The latter figure shows that the vertical displacements obtained by the direct integration of the observed axial strains match the displacements resulting from the FE model that reproduces the axial strains.

Figure 10 (a) shows the calculated shaft friction, SF, profiles for the three selected load cases as these were determined from the FE analysis. Again, these were obtained from the FE model that was calibrated to reproduce accurately the monitored axial strain and vertical displacements from FOs (see Figure 9). Furthermore, Figure 10(b)(c) show the evolution of SF with the applied load, P, and the ‘local’ vertical displacement, u, at three selected depths along the pile, according to the local soil stratigraphy, i.e. in the shallow layers (covered with pile casing), Lambeth Group and Thanet Sand. It is firstly observed that the first layer, which is covered by the pile casing does not show significant development of strains and approximately reaches an ultimate value of SF of about 40kPa. In contrast, Lambeth Group and Thanet Sand do exhibit a larger development of SF that reaches around 200kPa and 110kPa respectively. This difference was expected as the pile in the latter two layers was not covered with a steel casing and therefore pile-soil interaction friction develops resisting the pile movement. In general, as expected, the SF development curves show an initial stiffness that drops with the displacement, due to the plastic deformation of the soil close to the pile shaft. Finally, it is again shown that SF is mobilised early in the test, whereas the pile base pressure in mobilised at later stages for higher loads.

Finally, Figure 10 (d) shows the relevant design t-z and q-z curves following the API (2002) methodology. Although there are some differences between the observed (Figure 10 (c)) and design (Figure 10 (d)) curves, in general they seem to agree quite well yielding comparable values of ultimate pile shaft resistance.

4.3. Remarks

Using Eq. 9 – Eq. 12 and the geotechnical data in Figure 8 one would obtain an ultimate value of shaft capacity of 29kPa for the first layer (using Eq. 10), 32-219kPa for the second layer (using Eq. 9) and about 116kPa for the third layer (using Eq. 10). These values compare very well with the observed values from FO in Figure 10, which suggest around 30kPa, 200kPa and 110kPa for the three layers.

If one was to back calculate the values of α and β, then, the first layer would yield a value of $\beta=0.21$ (whereas Eq. 10 yields around $\beta=0.2$), layer 2 would yield a values of $\alpha=0.8$ (whereas the common assumption is 0.5 (Tomlinson 1997)) and the third layer a value of $\beta=0.2$ (in agreement to Eq. 10 that yields around $\beta=0.2$ too). So, in the case, the β-method seems to work well, whereas the appropriate value for α is slightly larger than the commonly used (0.5).

Similarly, when calculating the ultimate base capacity, one would obtain about 27MPa using Eq. 12 (i.e. based on c and φ) which is well above the (roughly linear) 12MPa that was observed from the FOs during this test. Again, the relation for the base capacity seems to overestimate significantly the observed pile base capacity.

5. Case study 3: Osterberg-cell pile test at Francis Crick Institute, London.

5.1. Description of pile test

This particular case study focuses on the behaviour of a 31.5m-long, 1500mm diameter bored pile during a preliminary load test at the Francis Crick Institute. This is a biomedical research centre situated next to St. Pancras International train station in the London Borough of Camden. One of the key differences from the previous case studies is the loading mechanism. Bi-directional Osterberg Cells (O-Cell) (Osterberg 1984) were used to apply load from the bottom of the pile. Figure 11(a) shows the geometry of the pile and the local stratigraphy; the ground consists of two thick layers of London Clay and Lambeth Group, with varying undrained strength, overlying Thanet Sand.

Similar to the previous case study, Fujikura reinforced ribbon cable (JBT-03813) and 8 core single mode fibre (205-301 Excel OS1 8C 9/125 Loose Tube LSOH Black) were used for measuring strain and temperature respectively. The installation process was identical to case study 1 where both fibre optic cables were routed along opposite sides of the reinforcement cage from the pile head to the top of O-Cell where a 10m long reference loop was located. A pre-strain of $2000\mu\varepsilon$ was induced in the strain cable during installation. Anchorage was provided by IC-ROC clamps manufactured by Fujikura. To serve as a comparison, 5 levels of VWSG were installed at 5 levels along the pile depth. The pile test consisted of a single load cycle reaching a maximum of 8.33MN after 7 loading steps and then unloading to zero after 3 steps, as shown in Figure 11 (b).

5.2. Data Interpretation

Figure 12(a) shows the measured axial strain profiles of the pile for three selected load stages from FO and VWSGs. Considering firstly the VWSGs only, it is shown that, as expected, large values of strain occur at the bottom of the pile (close to the O-cell) and smaller values occur at the top. Interestingly, at a depth of about 19m, there is a significantly higher value of VWSG strain which, in practice, could be considered as not representative of the actual strains in the pile and therefore ignored and discarded by the design engineers.

Eliminating outliers that do not conform to the expected ranges is common in data interpretation as instrument malfunctions do occur occasionally. Signs of VWSG malfunction may not always be clear and these anomalies can be caused by a number of scenarios such as cable damage. In some cases the recorded data is in fact a true representation which can be attributed to changes in ground conditions and construction quality.

However, it is observed that the fibre optic cable picks some unexpectedly high values of strain at a depth of about 18-23m. This is unexpected when the pile diameter is uniform at that depth and therefore no step is expected in the axial strains. The data indicates that the pile sustained high localised strains in that region. Similarities in trend for both systems triggered a further investigation into the soil strata where the nearest borehole log (BH04) (distance ~10m) recorded a change in soil layers from lignite beds and lower mottled beds in the Lambeth group at around 18-19m depth. Although such a scenario was not reported in the construction records, the presence of sandy glauconitic clay may have caused a localised collapse during the construction of the pile which may have caused necking of the pile (smaller cross-section). Subsequently, the cross sectional area, A, as well as the integrity of the concrete (e.g. Young's modulus, E) at this location would have been compromised. Therefore, a much higher strain reading would be very likely ($\varepsilon_a = F_a/EA$).

Computing the axial force by multiplying the axial strains with a constant axial stiffness, EA, would therefore be unrealistic. Here, a FE model was employed again in which the axial rigidity, EA, of the pile was kept constant along the pile depth, except at depth of 18-23m at which it was reduced. After a parametric study, it was found that, when EA at that location was reduced down to 35% of the initial EA (using again E=30000MPa and $A=0.25\pi d^2$, where d is the design diameter shown in Figure 11), a good match was obtained between the axial strains (Figure 12 (a)) and the vertical displacements (Figure 12 (c)). This apparent reduction in EA could be due to some pile necking (smaller A) or some mixing of the pile concrete with adjacent ground materials (smaller E). Then, using the results of the FE model, the axial force profiles in the pile were calculated by multiplying the axial strains by

EA everywhere except at depth 18-23m where 0.35EA was used. The latter profiles are shown in Figure 11 (b) along with the axial force from the FE model. It is shown that a good comparison was obtained between the two monitoring instruments and the relevant numerical analysis. As it may be observed the axial force profiles with the non-uniform EA vary smoothly with the depth (in contrast to the axial strain profiles) and this is expected because of force equilibrium (since the soil spring stiffness values have not been changed). It is appreciated here that the use of 0.35EA for the pile analysis is not ideal and it was literally obtained from a back-analysis matching the observed strain profiles. Perhaps another option would be to conduct a series of solid FE analyses (e.g. 2D axisymmetric) which consider different values of reduced E (of blended concrete and soil) and reduced A (i.e. reduced d^2).

Figure 13 (a) shows the calculated shaft friction, SF, profiles for the three chosen values of applied load, from the FE analysis. Again, these were obtained from the FE model that reproduced accurately the monitored axial strain and vertical displacements from FOs (see Figure 12). Furthermore, Figure 13(b)(c) show the evolution of SF with the applied load, P, and the 'local' vertical displacement, u, at two selected depths along the pile, according to the local soil stratigraphy, i.e. in the London Clay and the Lambeth Group. It is shown that Lambeth Group which is deeper and closer to the O-cell exhibits early development of shaft friction with the applied load, P, and that it has a stiffer response than the upper London Clay, which seems to reach a SF plateau of about 35kPa at about 0.01m displacement. In contrast, Lambeth Group shows an increasing development of SF which has not reached an ultimate value in this test.

Finally, Figure 13 (d) shows the relevant design t-z curves following the API (2002) methodology. Once again, although there are some differences between the observed (Figure 13 (c)) and design (Figure 13 (d)) curves, in general they seem to agree quite well providing similar values of ultimate pile shaft resistance.

5.3. Remarks

The monitoring data from the FO cables agree very well with the monitoring data from the VWSG. Moreover, the continuity of the FO data is able to highlight a region of localised high strain development which spreads over 6-8m in the pile shaft. A high value of strain was also captured by the VWSG sensors at the same depth, but as this was only a single value it could easily have been ignored and its significant difference from the other data points be erroneously attributed to instrument malfunction. However, the presence of continuous FO data here was able to support the localised high values of strain which might be due to some low quality concrete material of the pile or some mixing of ground material with pile concrete.

Moreover, the availability of these monitoring data allows the derivation of shaft friction development curves with the applied load or vertical displacement. These curves show that the developed shaft friction in the deeper soil layers (e.g. Lambeth Group), i.e. closer to the O-cell is, as expected, higher than the corresponding friction at the top of the pile, close to the ground surface.

Using Eq. 9 (i.e. based on S_u) and the geotechnical data in Figure 11 one would obtain an ultimate value of shaft capacity of 23-98kPa for the first layer and about 100-121kPa for the second layer. These values compare well with the observed values from FO in Figure 13, which suggest average values of around 30kPa and 150kPa for the two layers. It is shown that the shaft friction values interpreted from the observed FO data are very close to the expected design based on Eq. 9. Finally, if one was to back calculate the values of α in Eq. 9, then, the two layers would yield values of α=0.25 and α=0.68 respectively (whereas the common assumption is 0.5 (Tomlinson 1997)).

6. Conclusions

This paper presents the application of distributed fibre optic strain measurement technology for monitoring the actual field behaviour of axially loaded piles. The fibre optic data from three representative case studies of pile load tests conducted recently in London are analysed and compared to spatially-discrete point VWSGs and relevant simple finite-element analyses. The main findings of this study are the following:

- The BOTDR distributed monitoring system is able to provide a continuous profile of the induced strain within piles and this offers more confidence in determining the developed shaft friction profiles along the pile. It is also shown that the availability of continuous strain measurements offers a clear view of the condition of the entire pile and hence provides an indication of any localised regions of weakness, shaft area inhomogeneity or strain concentration. This is clearly a limitation of discrete monitoring systems such as VWSG, which do not provide adequate information for the whole length of the pile.

- The distributed FO data can provide reliable information about vertical pile displacements by direct integration of the spatially-continuous strain data. The calculated displacements from the FO strains were verified against the displacements obtained from a relevant FE model. It was found that such vertical displacement profiles are very useful in calibrating the model parameters of a FE model.

- An available and reliable set of monitoring data over the whole length of the pile allows an estimation of the shaft friction development curves with the applied load or vertical displacement (load-transfer) which may be used in future design of piles in a similar geographical region and soil stratigraphy.

- The obtained values of shaft friction and base resistance were compared with expected values from existing methods of geotechnical design (e.g. α and β-methods) and were generally found to be in good agreement. The “observed” values of α and β were back-analysed and were also found to be, in general, in good agreement with the suggested values from the literature.

- The obtained load-transfer (t-z and q-z) curves were compared with design curves from the literature (API). Although notable differences were observed regarding the pile base curves, the pile shaft curves were generally in good agreement.

Acknowledgements

This research was conducted within the Centre for Smart Infrastructure and Construction (CSIC) of the University of Cambridge, funded by EPSRC and Innovate UK. Their financial assistance is gratefully acknowledged. Also, the assistance of the CSIC team is acknowledged, including Professor Lord Robert Mair, Dr Jennifer Schooling, Peter Knott, Jason Shardelow and Jules Birks. Finally, the Authors would like to acknowledge the contribution of the numerous CSIC Industry partners, especially ARUP (Duncan Nicholson, Paul Morrison, Stuart Pennington), Cementation Skanska (Andrew Bell, Martin Pedley, Rab Fernie) and Laing O'Rourke.

Nomenclature

A – pile cross-sectional area

C_E – optical fibre parameter

C_T – optical fibre parameter

C_{TT} – optical fibre parameter

d – nonlinear model degradation parameter

D – pile diameter

E – pile Young's modulus

F_a – axial pile force

h – nonlinear model hardening parameter

k_m – nonlinear model maximum subgrade modulus parameter

L – total length of pile

M – optical fibre strain coefficient

N – optical fibre temperature coefficient

N_c – pile end bearing capacity factor

n_f – fibre core refractive index

P – top load value

q_b – pile base pressure

r – pile radius

SF – shaft friction

S_u – undrained soil shear strength

t – nonlinear model shear stress parameter

t_m – nonlinear model maximum shear stress parameter

u – vertical displacement

v_α – acoustic velocity in the optical fibre

v_b – central Brillouin frequency

v_{b0} – central Brillouin frequency at zero strain and temperature difference

y – depth

z – local vertical displacement

α – adhesion factor

ΔT – temperature change

Δv_{bS} – Brillouin frequency change reading from “strain cable”

Δv_{bT} – Brillouin frequency change reading from “temperature cable”

γ – soil unit weight

ε_{a} – axial pile strain

ε_{mech} – mechanical strain

ε_{real} – real (observed) strain

ε_{temp} – thermal expansion strain

λ_{I} – wavelength of the input light

v – Poisson’s ratio

References

Abchir, Z, Burlon, S, Frank, R, Habert, J & Legrand, S 2015, 't–z curves for piles from pressuremeter test results', *Géotechnique*, vol 66, no. 2, pp. 137-148.

Acikgoz, MS, Pelecanos, L, Giardina, G, Aitken, J & Soga, K 2017, 'Distributed sensing of a masonry vault during nearby piling', *Structural Control and Health Monitoring*, vol 24, no. 3, p. e1872.

Acikgoz, MS, Pelecanos, L, Giardina, G & Soga, K 2016, 'Field monitoring of piling effects on a nearby masonry vault using distributed sensing.', *International Conference of Smart Infrastructure and Construction*, ICE Publishing, Cambridge.

API 2002, 'API Recommended Practice. Planning, Designing and Constructng Fixed Offshore Platforms - Working Stress Design', American Petroleum Institute, 2A-WSD, American Petroleum Institute.

Bathe, KJ 1996, *Finite Element Procedures*, 1st edn, Prentice Hall, New Jersey.

Berezantzev, VG, Khristoforov, VS & Golubkov, VN 1961, 'Load bearing capacity and deformation of piled foundations', *Proc. 5th Int. Conf. on Soil Mechanics and Foundation Engineering*, Paris.

Bustamante, M & Gianeselli, L 1982, 'Pile bearing capacity predictions by means of static', *Proc., 2nd European Symp. on Penetration Testing*, Amsterdam.

Butterfield, R & Banergee, PK 1971, 'The elastic analysis of compressible piles and pile groups', *Geotechnque*, vol 21, no. 1, pp. 43-60.

Cheung, L, Soga, K, Bennett, PJ, Kobayashi, Y, Amatya, B & Wright, P 2010, 'Optical fibre strain measurement for tunnel lining monitoring', *Proceedings of the ICE - Geotechnical Engineering*, vol 163, no. 3, pp. 119-130.

Comodromos, EM & Bareka, SV 2009, 'Response evaluation of axially loaded fixed-head pile groups in clayey soils', *International Journal for Numerical and Analytical Methods in Geomechanics*, vol 33, no. 17, pp. 1839-1865.

de Battista, N, Elshafie, MZEB, Soga, K, Williamson, M, Hazelden, G & Hsu, YS 2015, 'Strain monitoring using embedded distributed fibre optic sensors in a sprayed concrete tunnel lining during the excavation of cross-passages', 7th International Conference on Structural Health Monitoring and Intelligent Infrastructure (SHMII7), Torino, Italy.

de Battista, N, Kechavarzi, C, Seo, H, Soga, K & Pennington, S 2016, 'Distributed fibre optic sensors for measuring strain and temperature of cast-in-situ concrete test piles', *Proceedings of the International Conference on Smart Infrastructure and Construction (ICSIC)*, Thomas Telford, Cambridge, UK.

Di Murro, V, Pelecanos, L, Soga, K, Kechavarzi, C, Morton, RF & Scibile, L 2016, 'Distributed fibre optic long-term monitoring of concrete-lined tunnel section TT10 at CERN.', *International Conference of Smart Infrastructure and Construction*, ICE Publishing, Cambridge.

Doherty, P, Igoe, D, Murphy, G, Gavin, K, Preston, J, McAvoy, C, Byrne, BW, McAdam, R, Burd, HJ, Houlsby, GT, Martin, CM, Zdravkovic, LT, Taborda, DMG, Potts, DM, Jardine, RJ, Sideri, M, Schroeder, FC, Muir Wood, A, Kallehave, D & Skov Gretlund, J 2015, 'Field validation of fibre Bragg grating sensors for measuring strain on driven steel piles', *Géotechnique Letters*, vol 5, no. 2, pp. 74-79.

Eslami, A & Fellenius, BH 1997, 'Pile capacity by direct CPT and CPTU methods applied to 102 case histories', *Can. Geotech. J*, vol 34, pp. 886-904.

Fellenius, BH 1989, 'Prediction of pile capacity', *ASCE Symposium on Predicted and Observed Behavior of Piles*.

Frank, R & Zhao, SR 1982, 'Estimating the Settlement of Axially Loaded Bored Piles in Fine Sand by PMT Data', *Bull. Liaison LPC*, vol 119.

Goldfeld, Y & Klar, A 2013, 'Damage Identification in Reinforced Concrete Beams Using Spatially Distributed Strain Measurements', *Journal of Structural Engineering*, vol 139, no. 12, pp. 1-11.

Hauswirth, D, Puzrin, AM, Carrera, A, Standing, JR & Wan, MSP 2014, 'Use of fibre-optic sensors for simple assessment of ground surface displacements during tunnelling', *Geotechnique*, vol 64, no. 10, pp. 837-842.

Horiguchi, T, Shimizu, K, Kurashima, T, Tateda, M & Koyamada, Y 1995, 'Development of a distributed sensing technique using Brillouin scattering', *Journal of Light-wave Technology*, vol 13, no. 7, pp. 1296-1302.

Iten, M 2011, 'Novel applications of distributed fiber-optic sensing in geotechnical engineering', PhD Thesis, ETH, Zurich.

Jardine, RJ & Chow, FC 1996, 'New design methods for offshore piles', MTD, Centre for Petroleum and Marine Technology (CPMT), 96/103, London.

Kechavarzi, C, Soga, K, de Battista, N, Pelecanos, L, Elshafie, MZEB & Mair, RJ 2016, *Distributed Fibre Optic Strain Sensing for Monitoring Civil Infrastructure*, Thomas Telford, London.

Kersey, AD & Morey, WW 1993, 'Multiplexed Bragg grating fibre-laser strain-sensor system with mode-locked interrogation', *Electron. Lett*, vol 29, no. 1, pp. 112-114.

Kitiyodom, P & Matsumoto, T 2003, 'A simplified analysis method for piled raft foundations in non-homogeneous soils.', *International Journal for Numerical and Analytical Methods in Geomechanics*, vol 27, pp. 85-109.

Klar, A, Bennett, PJ, Soga, K, Mair, RJ, Tester, P, Fernie, R, St John, HD & Thorp-Peterson, G 2006, 'Distributed strain measurement for pile foundations', *Proceedings of the ICE - Geotechnical Engineering*, vol 159, no. 3, pp. 135-144.

Klar, A, Dromy, I & Linker, R 2014, 'Monitoring tunneling induced ground displacements using distributed fiber-optic sensing', *Tunnelling and Underground Space Technology*, vol 40, pp. 141-150.

Knappett, JA & Craig, RF 2012, *Craig's Soil Mechanics*, 8th edn, CRC Press, London.

Kraft, ML, Ray, RP & Kakaaki, T 1981, 'Theoretical t-z curves', *J. Geotech. Engrg. Div. ASCE*, vol 107, no. 11, pp. 1543-1561.

Kulhawy, FH & Prakoso, WA 1999, 'Discussion of “End Bearing Capacity of Drilled Shafts in Rock', *J. Geotech Eng ASCE*, vol 125, no. 12, pp. 1106-1109.

Kurashima, T, Horiguchi, T, Izumita, H & Tateda, M 1993, 'Brillouin Optical-Fiber Time Domain Reflectometry', *IEICE Transactions on Cummunications*, vol E76-B, no. 4, pp. 382-390.

Lee, CY 1993, 'Pile group settlement analysis by hybrid layer approach', *Journal of the Geotechnical Engineering Division, ASCE*, vol 119, no. 6, pp. 984-997.

Lee, W, Lee, W, Lee, S & Salgado, R 2004, 'Measurement of pile load transfer using the Fiber Bragg Grating sensor system', *Canadian Geotechnical Journal*, vol 41, no. 6, pp. 1222-1232.

Lehane, BM, Jardine, RJ, Bond, AJ & R., F 1993, 'Mechanisms of shaft friction in sand from instrumented pile tests', *Journal of Geotechnical Engineering*, vol 119, no. 1, pp. 19-35.

Levenberg, K 1944, 'A Method for the Solution of Certain Non-Linear Problems in Least Squares', *Quarterly of Applied Mathematics*, vol 2, pp. 164-168.

Linker, R & Klar, A 2015, 'Detection of Sinkhole Formation by Strain Profile Measurements Using BOTDR: Simulation Study', *Journal of Engineering Mechanics*, pp. 1-10.

Liu, J & Zhang, M 2012, 'Measurement of residual force locked in open-ended pipe pile using FBG-based sensors', *Electron. J. Geotech. Eng*, vol 17, pp. 2145-2154.

Marduardt, D 1963, 'An Algorithm for Least-Squares Estimation of Nonlinear Parameters', *SIAM Journal on Applied Mathematics*, vol 11, no. 2, pp. 431-441.

McCabe, BA & Lehane, BM 2006, 'Behavior of Axially Loaded Pile Groups Driven in Clayey Silt', *Journal of Geotechnical and Geoenvironmental Engineering*, vol 132, no. 3, pp. 401-410.

Ménard, L 1963, 'Calcul de la force portante des fondations à partir des essais pressiométriques', *Sols-Soils*, vol 6, pp. 9–27.

Meyerhof, GG 1965, 'Shallow foundations', *Journal of Soil Mechanics and Foundations Division, ASCE*, vol 91, no. 2, pp. 21-31.

Mohamad, H 2007, 'Distributed optical fibre strain sensing of geotechnical structures. PhD Thesis', University of Cambridge, Cambridge, UK.

Mohamad, H, Bennett, PJ, Soga, K, Mair, RJ & Bowers, K 2010, 'Behaviour of an old masonry tunnel due to tunnelling-induced ground settlement', *Geotechnique*, vol 60, no. 12, pp. 927-938.

Mohamad, H, Soga, K, Bennett, PJ, Mair, RJ & Lim, CS 2012, 'Monitoring Twin Tunnel Interaction Using Distributed Optical Fiber Strain Measurements', *Journal of Geotechnical and Geoenvironmental Engineering*, vol 138, no. 8, pp. 957-967.

Mohamad, H, Soga, K, Pellew, A & Bennett, PJ 2011, 'Performance Monitoring of a Secant-Piled Wall Using Distributed Fiber Optic Strain Sensing', *Journal of Geotechnical and Geoenvironmental Engineering, ASCE*, vol 137, no. 12, pp. 1236-1243.

Osterberg, JO 1984, 'A new simplified method for load testing drilled shafts', *Foundation Drilling*, ADSC.

Ouyang, Y, Broadbent, K, Bell, A, Pelecanos, L & Soga, K 2015, 'The use of fibre optic instrumentation to monitor the O-Cell load test on a single working pile in London', *Proceedings of the XVI European Conference on Soil Mechanics and Geotechnical Engineering*, Edinburgh.

Pelecanos, L & Soga, K 2017, 'Using distributed strain data to evaluate load-transfer curves for axially loaded piles', *Journal of Geotechnical & Geoenvironmental Engineering, ASCE (Submitted)*.

Pelecanos, L, Soga, K, Chunge, MPM, Ouyang, Y, Kwan, V, Kechavarzi, C & Nicholson, D 2017, 'Distributed fibre-optic monitoring of an Osterberg-cell pile test in London.', *Geotechnique Letters*, vol 7, no. 2, pp. 1-9.

Pelecanos, L, Soga, K, Hardy, S, Blair, A & Carter, K 2016, 'Distributed fibre optic monitoring of tension piles under a basement excavation at the V&A museum in London.', *International Conference of Smart Infrastructure and Construction*, ICE Publishing, Cambridge.

Poulos, HG 1989, 'Pile behaviour - theory and application', *Geotechnique*, vol 39, no. 3, pp. 365-415.

Poulos, HG & Davis, EH 1974, *Elastic solutions for soil and rock mechanics*, Wiley, New York.

Randolph, MF 2003, 'Science and empiricism in pile foundation design', *Geotechnique*, vol 53, no. 10, pp. 847-875.

Salgado, R 2008, *The engineering of foundations*, McGraw Hill, New York.

Savitzky, A & Golay, MJE 1964, 'Smoothing and Differentiation of Data by Simplified Least Squares Procedures', *Analytical Chemistry*, vol 36, no. 8, pp. 1627-1639.

Schwamb, T & Soga, K 2015, 'Numerical modelling of a deep circular excavation at Abbey Mills in London', *Geotechnique*, vol 65, no. 7, pp. 604-619.

Schwamb, T, Soga, K, Mair, RJ, Elshafie, MZEB, R., S, Boquet, C & Greenwood, J 2014, 'Fibre optic monitoring of a deep circular excavation', *Proceedings of the ICE - Geotechnical Engineering*, vol 167, no. 2, pp. 144-154.

Seo, H-J, Pelecanos, L, Kwon, Y-S & Lee, IM 2017, 'Net load–displacement estimation in soil-nail pullout tests', *Proceedings of the Institution of Civil Engineers - Geotechnical Engineering*, pp. 1-14.

Soga, K 2014, 'XII Croce Lecture: Understanding the real performance of geotechnical structures using an innovative fibre optic distributed strain measurement technology', *Rivista Italiana di Geotechnica*, vol 4, pp. 7-48.

Soga, K, Kechavarzi, C, Pelecanos, L, de Battista, N, Williamson, M, Gue, CY, Di Murro, V & Elshafie, M 2017, 'Distributed fibre optic strain sensing for monitoring underground structures - Tunnels Case Studies ', in S Pamukcu, L Cheng (eds.), *Underground Sensing*, 1st edn, Elsevier.

Soga, K, Kwan, V, Pelecanos, L, Rui, Y, Schwamb, T, Seo, H & Wilcock, M 2015, 'The role of distributed sensing in understanding the engineering performance of geotechnical structures', *Proceedings of the XVI European Conference on Soil Mechanics and Geotechnical Engineering*, Edinburgh.

Stas, CV & Kulhawy, FH 1984, 'Critical evaluation of design methods for foundation under axial uplift & compression loading', Electric Power Research Institute, EL-3771, Palo Alto.

Tomlinson, MJ 1997, 'The adhesion of piles driven in clay', *Proc. 4th Intern. Conf. Soil. Mech.*, London.

Tomlinson, M & Woodward, J 2014, *Pile design and construction practice*, CRC Press.

Appendix A

The numerical finite element analysis used in this paper is described in Figure 14. A vertical axially-loaded pile is modelled with a series of linear-elastic two-noded beam elements with vertical displacement degrees-of-freedom only and a series of nonlinear springs, representing the surrounding soil, attached to each node.

The behaviour of the soil spring is governed by a nonlinear load-transfer curve that follows the Degradation and Hardening Hyperbolic Model (DHHM) model of (Pelecanos & Soga 2017) described by Eq. 13.

$$t = \frac{k_m z}{\sqrt[d]{\left(1 + \left(\frac{k_m}{t_m} z\right)^{hd}\right)}}$$

Eq. 13

Where k_m is the maximum stiffness for displacement, z=0 (units: [force/length^3]), t_m is the "maximum" value of shear stress, t (maximum only in the case of no hardening/softening, i.e. h=0) (units: [force/length^2]), d is the degradation parameter (units: [-]), that governs the degradation of subgrade modulus, k, with displacement, z, and h is the hardening parameter (units: [-]), that mostly governs the model behaviour at large displacements, z. It should be noted here that some t-z curves (see Section 1) include the effect of the pile diameter too, but in the considered cases that mostly involved London Clay and large pile diameters (i.e. no significant arching) it is expected that the diameter doesn't affect the obtained t-z curves.

The values of the 4 parameters of the model (k_m, t_m, d, h) are obtained by matching the axial strain, $\varepsilon_a(z)$, and vertical displacement, u(z), profiles resulting from the numerical model and those observed in the field as shown in Figure 6 (a) (c), Figure 9 (a) (c) and Figure 12 (a) (c).

The equations satisfying global equilibrium of the pile-soil problem follow a standard static finite element formulation (Bathe 1996) and are described by Eq. 14.

$$\left[K_p + K_s\right] \cdot \{u\} = \{F\}$$

Eq. 14

Where, $[K_p]$ and $[K_s]$ are the global pile and soil stiffness matrices respectively, which contain information about the geometry and the material properties of the pile and soil respectively, {u} is the vector of the displacement degrees-of-freedom and {F} is the vector of the externally applied forces.

Boundary conditions applied consist only of the applied load which is specified as a known value in the {F} vector; at the first node for a top-loaded pile or at the last node for a bottom-loaded O-cell test. Finally, the numerical model parameters adopted for the analyses of the case studies presented in this paper (which, as explained before, were obtained by matching the observed pile response) are listed in Table 1.

Table 1. Parameters of the numerical FE beam-spring model for all cases considered

Case 1 – Broadgate Pile					
Layer	**Depth [m]**	**k_m [MN/m^3]**	**t_m [MN/m^2]**	**d []**	**h []**
1	0 – 6	8	0.011	2	0.8
2	6 – 12	14	0.157	0.9	1.5
3	12 – 19	16	0.136	2.5	1
4	19 – 25	2	0.008	1.2	1
Base	25	459	65573	1	1
Case 2 – East Village Pile					
Layer	**Depth [m]**	**k_m [MN/m^3]**	**t_m [MN/m^2]**	**d []**	**h []**
1	0 – 14	14	0.053	1	1
2	14 – 23	37	0.223	1	1
3	23 – 32	24	0.195	1.6	1
Base	32	513	17.113	1	1
Case 3 – Francis Crick Pile					
Layer	**Depth [m]**	**k_m [MN/m^3]**	**t_m [MN/m^2]**	**d []**	**h []**
1	0 – 21	21	0.036	3	1
2	1 – 25	57	0.117	3	0.7

Appendix B

The data used for the API (2002) curves shown in Figure 7, Figure 10, Figure 13 are listed in Table 2. These curves depend only on the soil material properties and the geometry (diameter, D) of the pile. The values for t_{ult} were obtained by using Eq. 9 and Eq. 10 for clay and sand respectively, whereas those for q_{ult} were obtained by using Eq. 11 and Eq. 12 for clay and sand respectively.

Table 2. Data used for the API (2002) curves.

t-z for sand								
z [in]	0	0.1	0.4					
t/t_{ult} [-]	0	1	1					
t-z for clay								
z/D [-]	0	0.0016	0.0031	0.0057	0.008	0.01	0.02	0.03
t/t_{ult} [-]	0	0.3	0.5	0.75	0.9	1	0.9	0.9
q-z for sand & clay								
z/D [-]	0	0.002	0.13	0.042	0.073	0.1	0.2	
$q/q_{\_ult}$	0	0.25	0.5	0.75	0.9	1	1	

Figure Captions

Figure 1. Principle of distributed fibre optic sensing using BOTDR.

Figure 2. Fibre optic cables used at the pile cases studied: (a) Fujikura reinforced “strain cable” and (b) Unitube “temperature cable”.

Figure 3. Schematic illustration of FO installation and monitoring of piled foundations.

Figure 4. View of installed fibre optic cables and vibrating wire strain gauges on the pile cage: (a) detailed view of clamp, (b) general view of installed sensors.

Figure 5. Description of Case 1 – Broadgate pile load test case: (a) pile geometry & soil stratigraphy, (b) test schedule

Figure 6. Monitored data profiles for Case 1 – Broadgate: (a) axial strain, (b) axial force and (c) vertical displacement.

Figure 7. Calculated pile shaft friction from FE analysis for Case 1 – Broadgate: (a) shaft friction profiles, (b) shaft friction development with applied load, (c) shaft friction development with vertical displacement, and (d) relevant API t-z and q-z curves.

Figure 8. Description of Case 2 – East Village pile load test case: (a) pile geometry & soil stratigraphy, (b) test schedule

Figure 9. Monitored data profiles for Case 2 – East Village: (a) axial strain, (b) axial force and (c) vertical displacement.

Figure 10. Calculated pile shaft friction from FE analysis for Case 2 – East Village: (a) shaft friction profiles, (b) shaft friction development with applied load, (c) shaft friction development with vertical displacement, and (d) relevant API t-z and q-z curves.

Figure 11. Description of Case 3 – Francis Crick pile load test case: (a) pile geometry & soil stratigraphy, (b) test schedule

Figure 12. Monitored data profiles for Case 3 – Francis Crick: (a) axial strain, (b) axial force and (c) vertical displacement.

Figure 13. Calculated pile shaft friction from FE analysis for Case 3 – Francis Crick: (a) shaft friction profiles, (b) shaft friction development with applied load, (c) shaft friction development with vertical displacement, and (d) relevant API t-z curves.

Figure 14. Numerical analysis model of pile-soil interaction: (a) pile, (b) axial strain distribution, (c) top load-displacement, (d) numerical beam-spring model and (e) load-transfer curve.

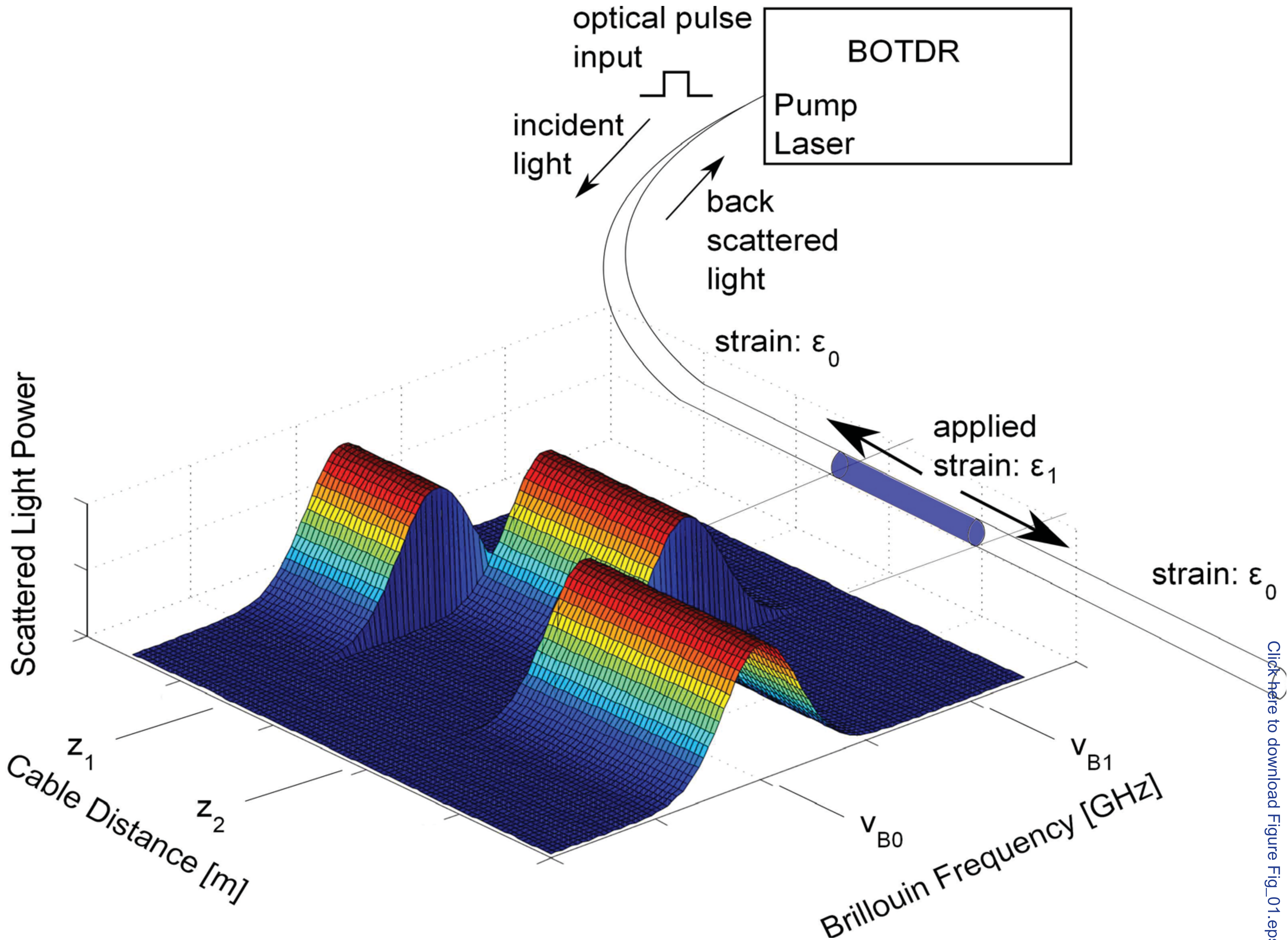

optical pulse input
BOTDR
Pump Laser
incident light
back scattered light
strain: ε0
applied strain: ε1
strain: ε0
Scattered Light Power
z1
z2
Cable Distance [m]
vB0
vB1
Brillouin Frequency [GHz]

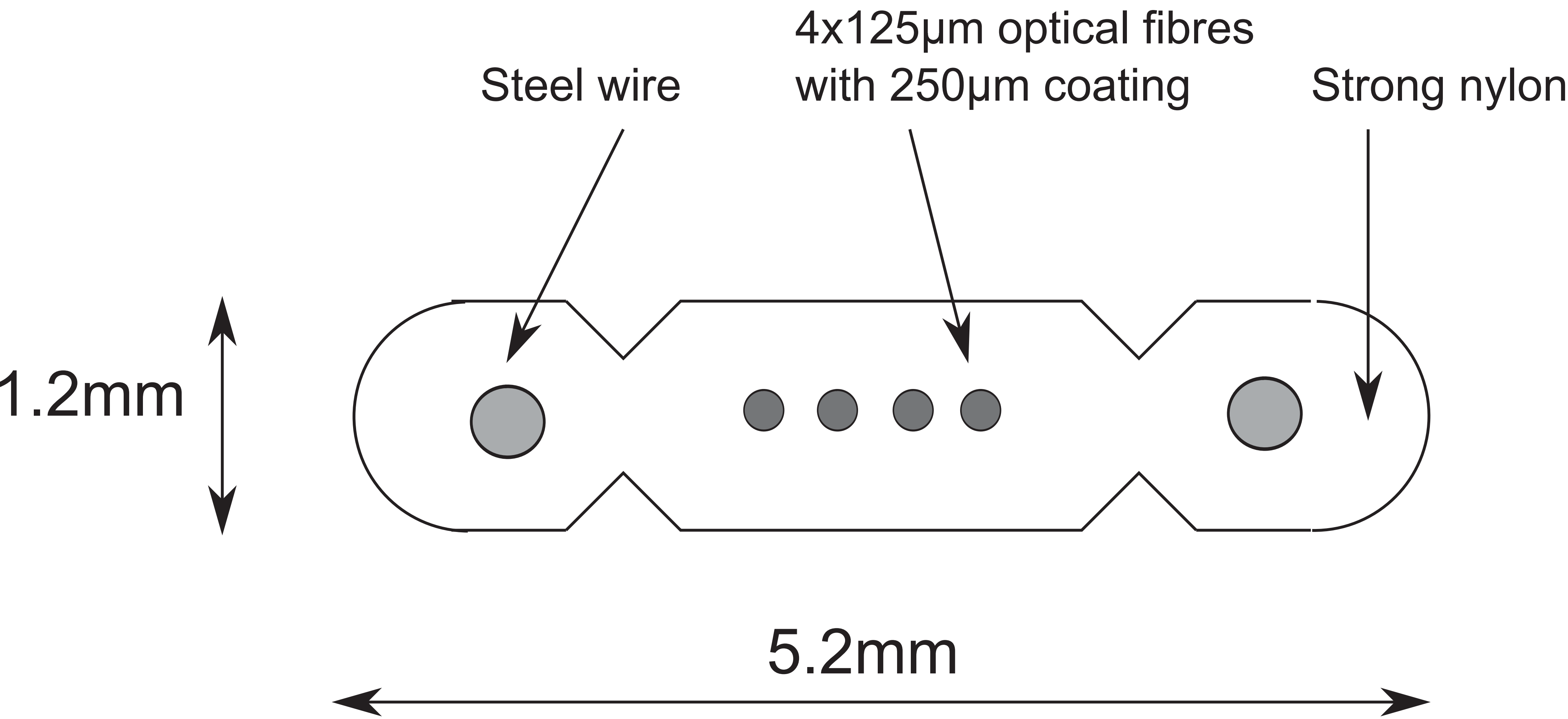
4x125µm optical fibres
with 250µm coating
Steel wire
Strong nylon
1.2mm
5.2mm

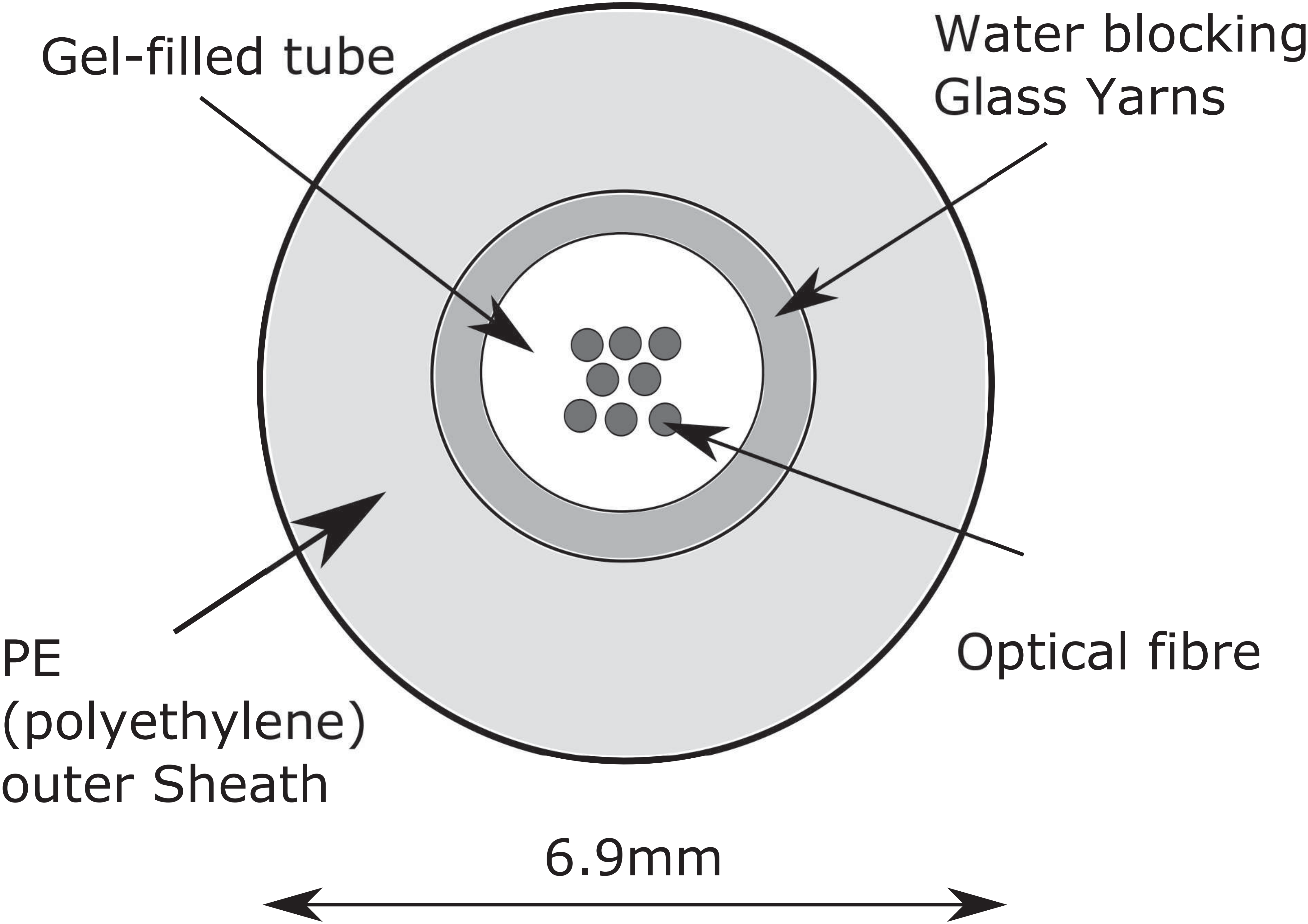
Gel-filled tube
Water blocking Glass Yarns
Optical fibre
PE (polyethylene) outer Sheath
6.9mm

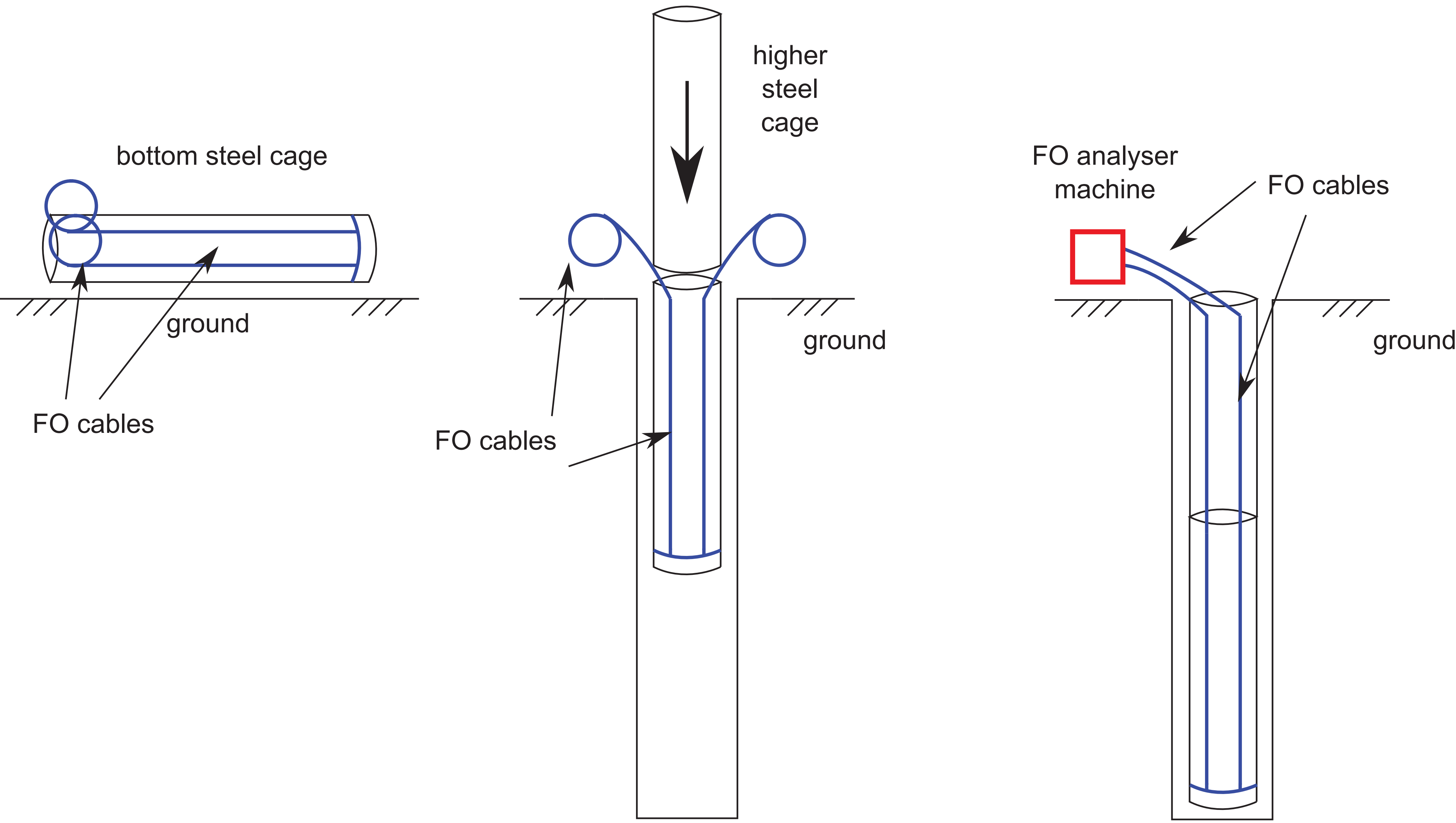

bottom steel cage
ground
FO cables
higher
steel
cage
FO cables
ground
FO analyser
machine
FO cables
ground

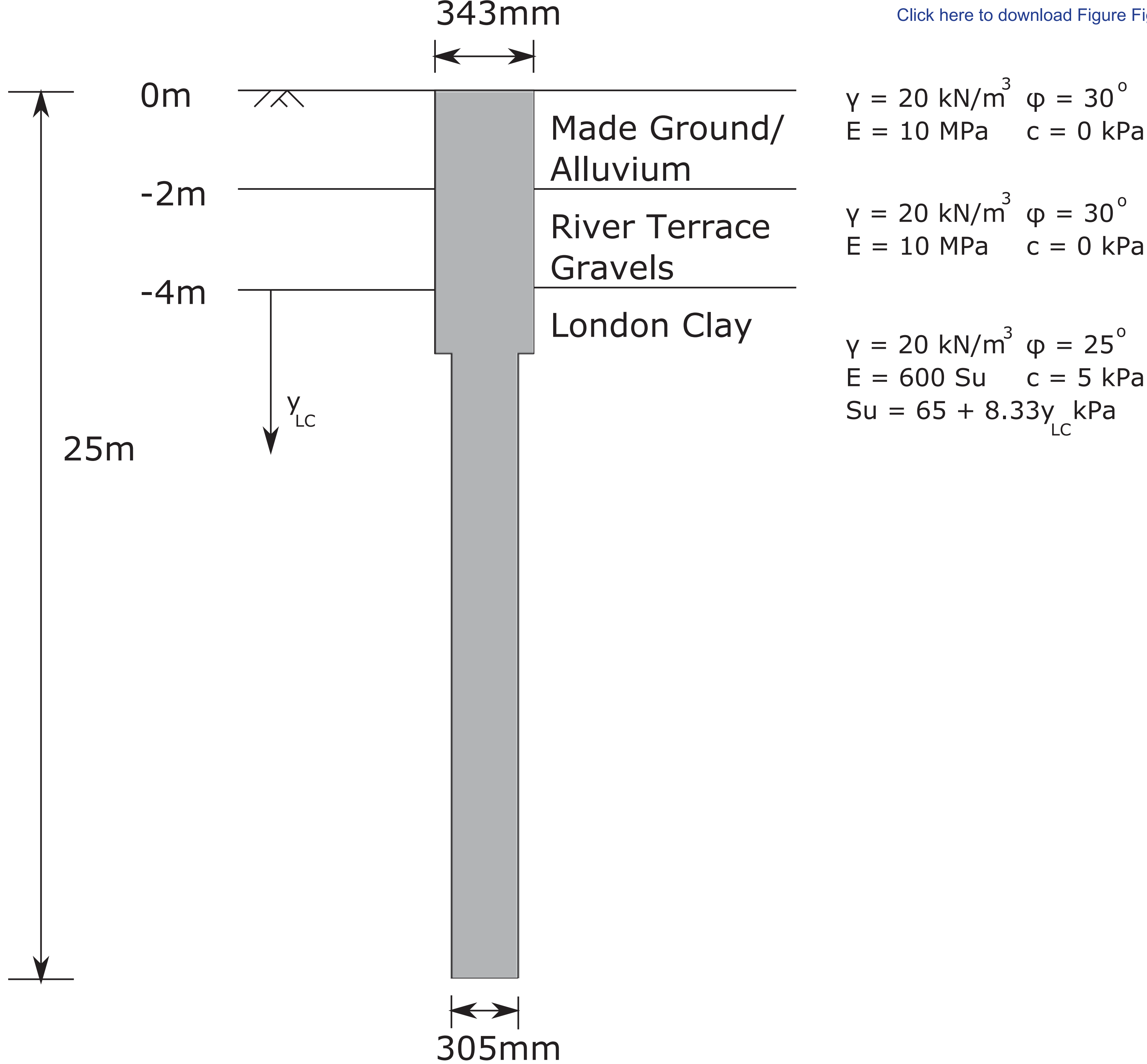
343mm
0m
-2m
-4m
25m
y
LC
Made Ground/
Alluvium
River Terrace
Gravels
London Clay
γ = 20 kN/m3 φ = 30o
E = 10 MPa c = 0 kPa
γ = 20 kN/m3 φ = 30o
E = 10 MPa c = 0 kPa
γ = 20 kN/m3 φ = 25o
E = 600 Su c = 5 kPa
Su = 65 + 8.33yLC kPa
305mm

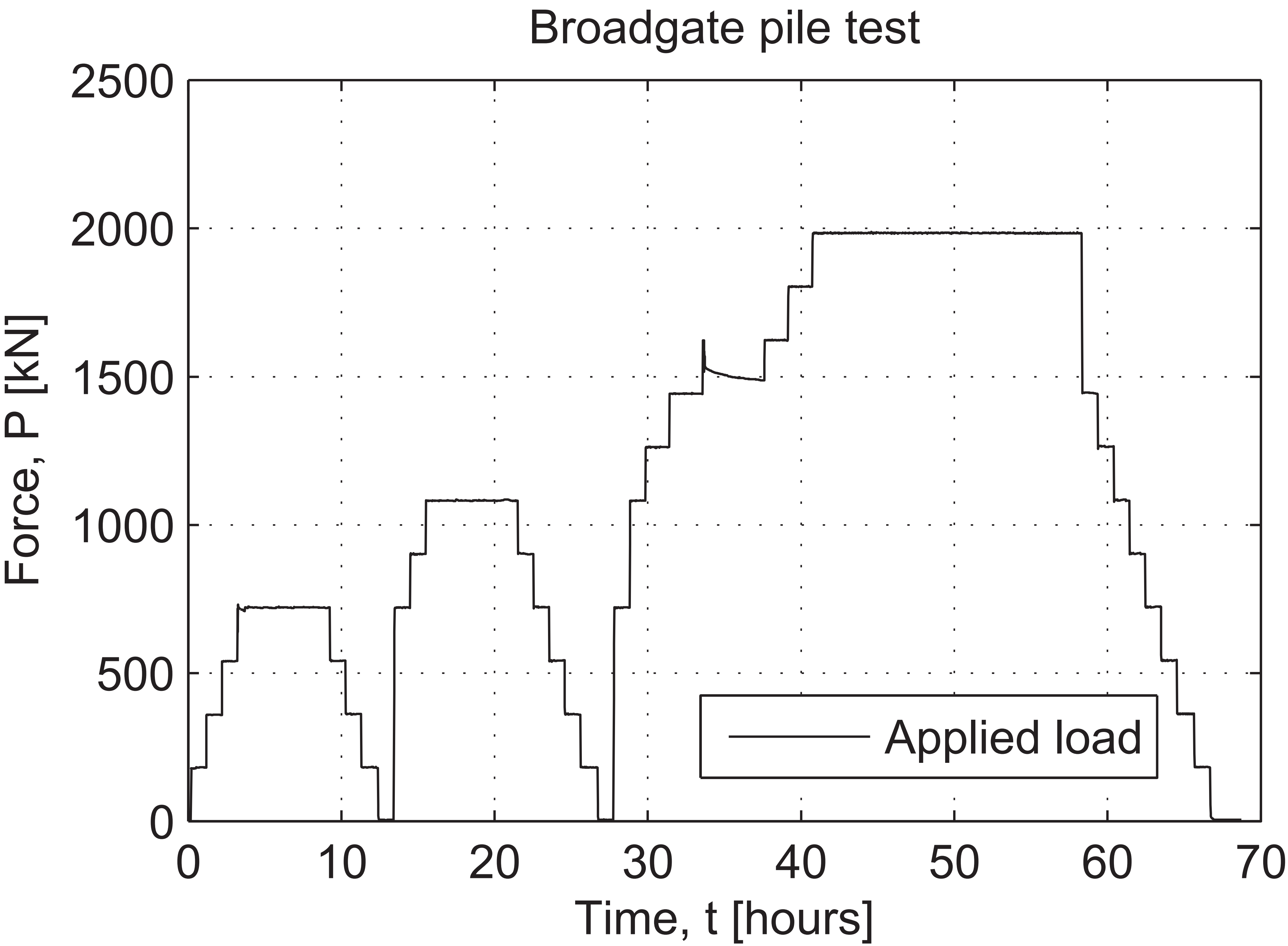
Broadgate pile test
Force, P [kN]
2500
2000
1500
1000
500
0
0
10
20
30
40
50
60
70
Time, t [hours]
Applied load

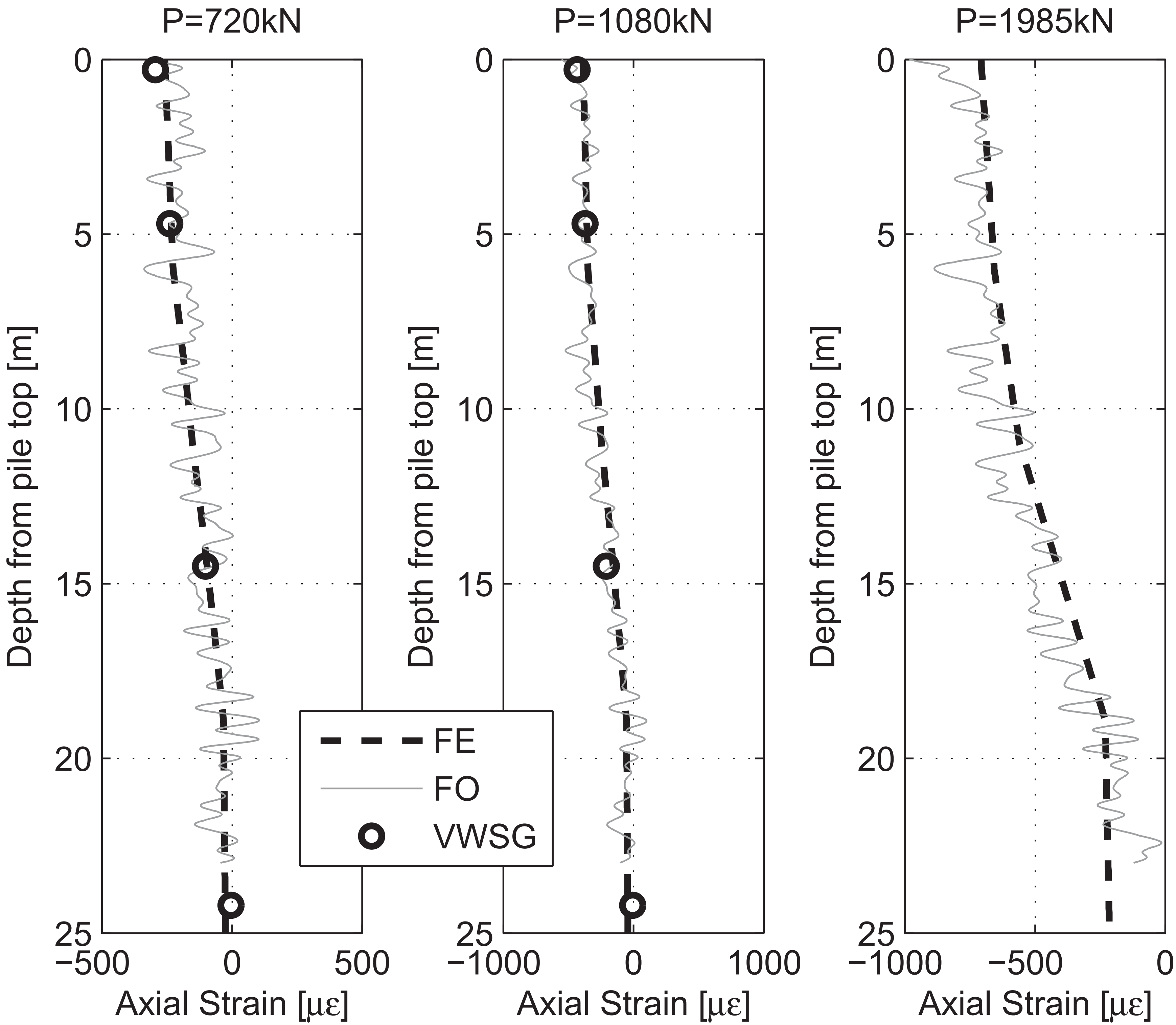
P=720kN
P=1080kN
P=1985kN
Depth from pile top [m]
0
5
10
15
20
25
−500
0
500
−1000
0
1000
−1000
−500
0
Axial Strain [με]
FE
FO
VWSG

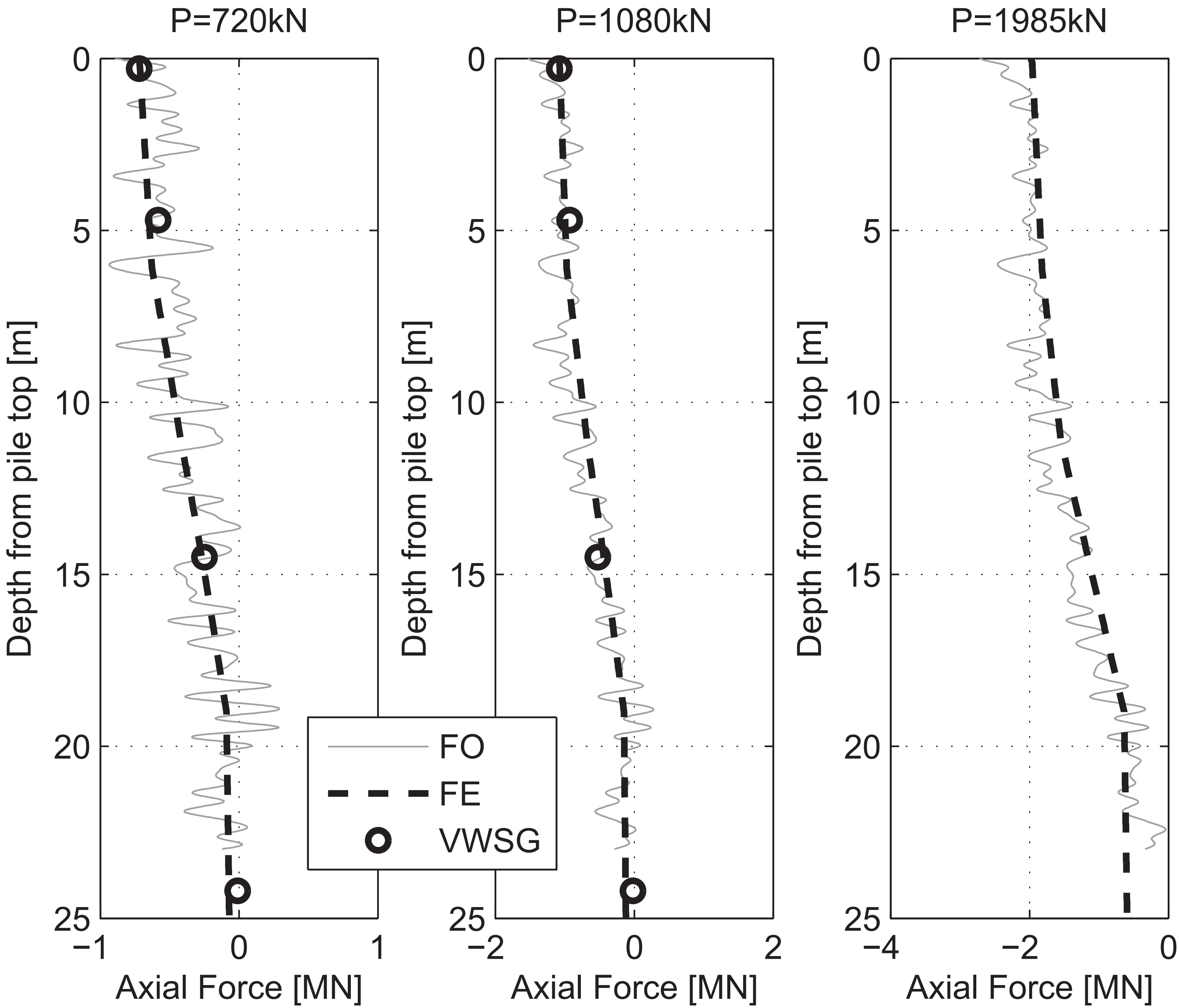
P=720kN
P=1080kN
P=1985kN
Depth from pile top [m]
0
5
10
15
20
25
−1
0
1
−2
0
2
−4
−2
0
Axial Force [MN]
FO
FE
VWSG

Click here to download Figure Fig_06c.eps

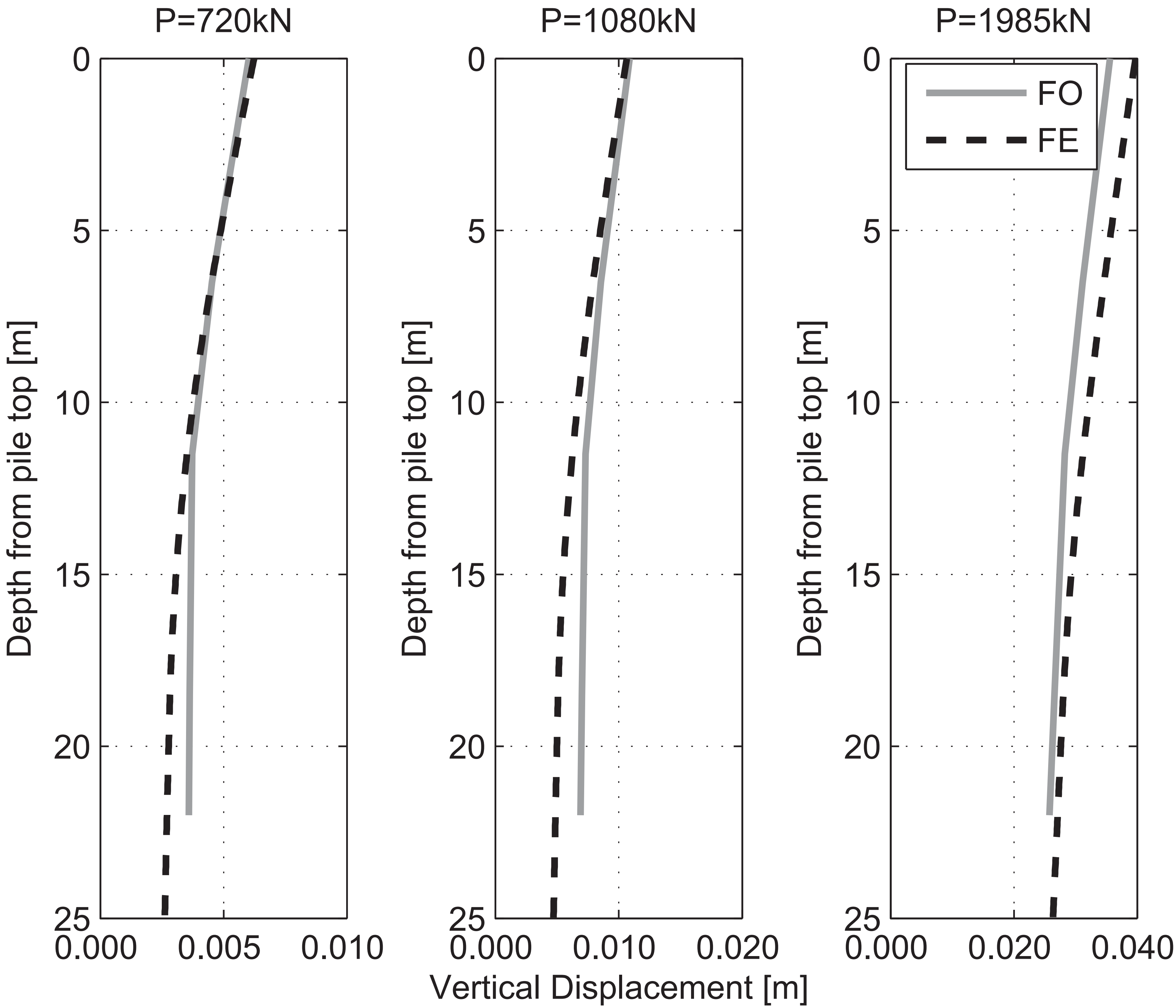

Click here to download Figure Fig_07a.eps

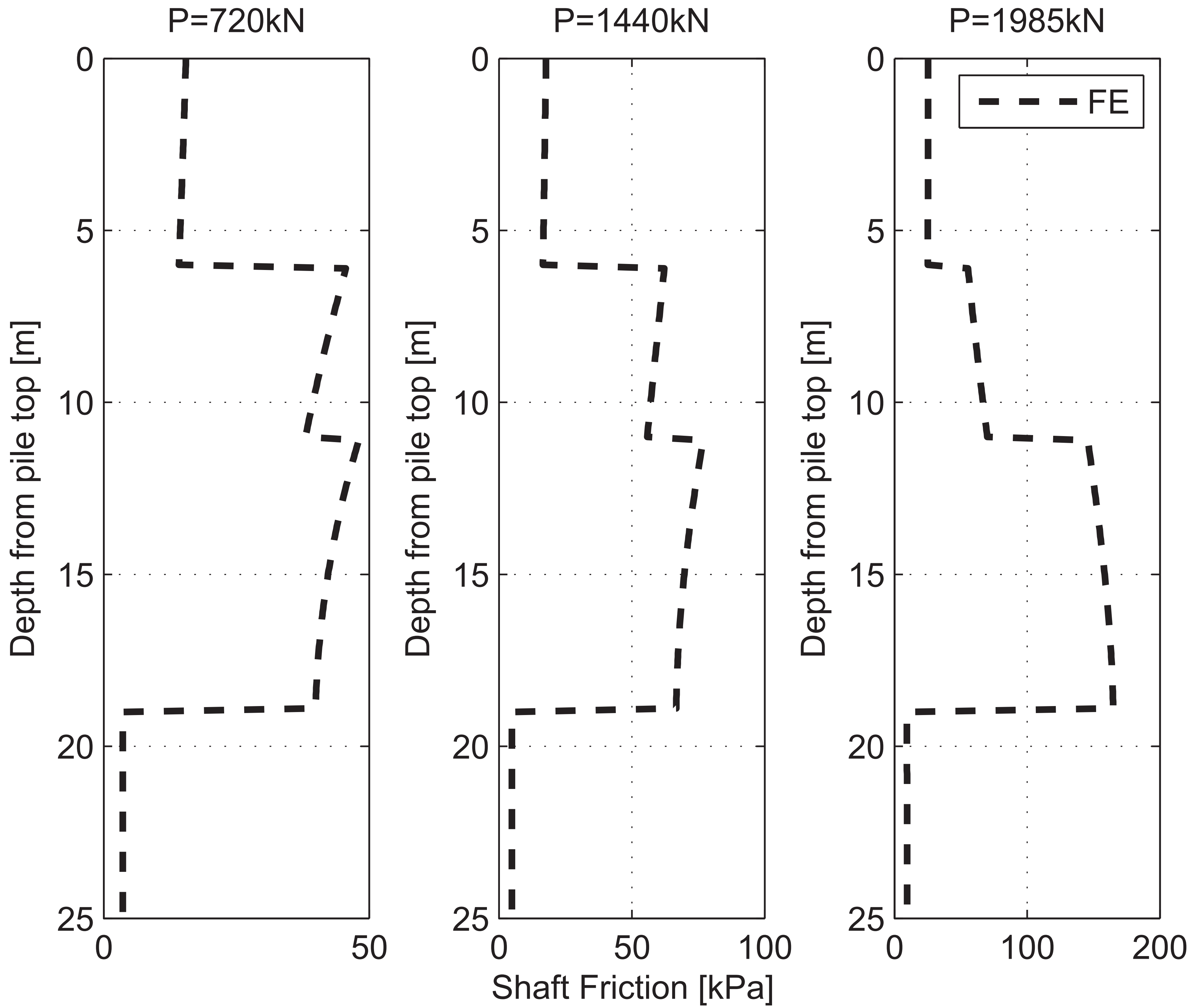

Click here to download Figure Fig_07b.eps

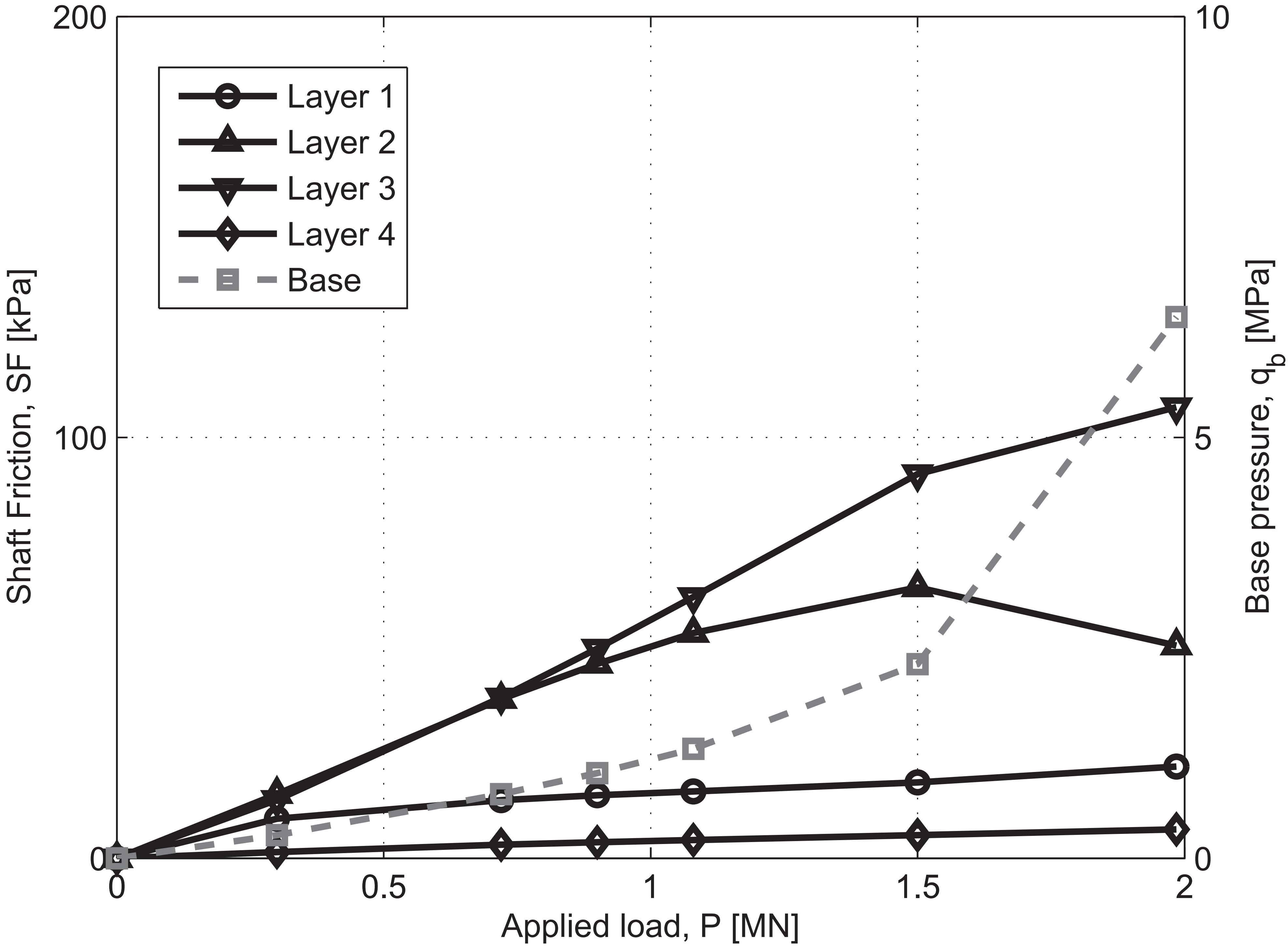

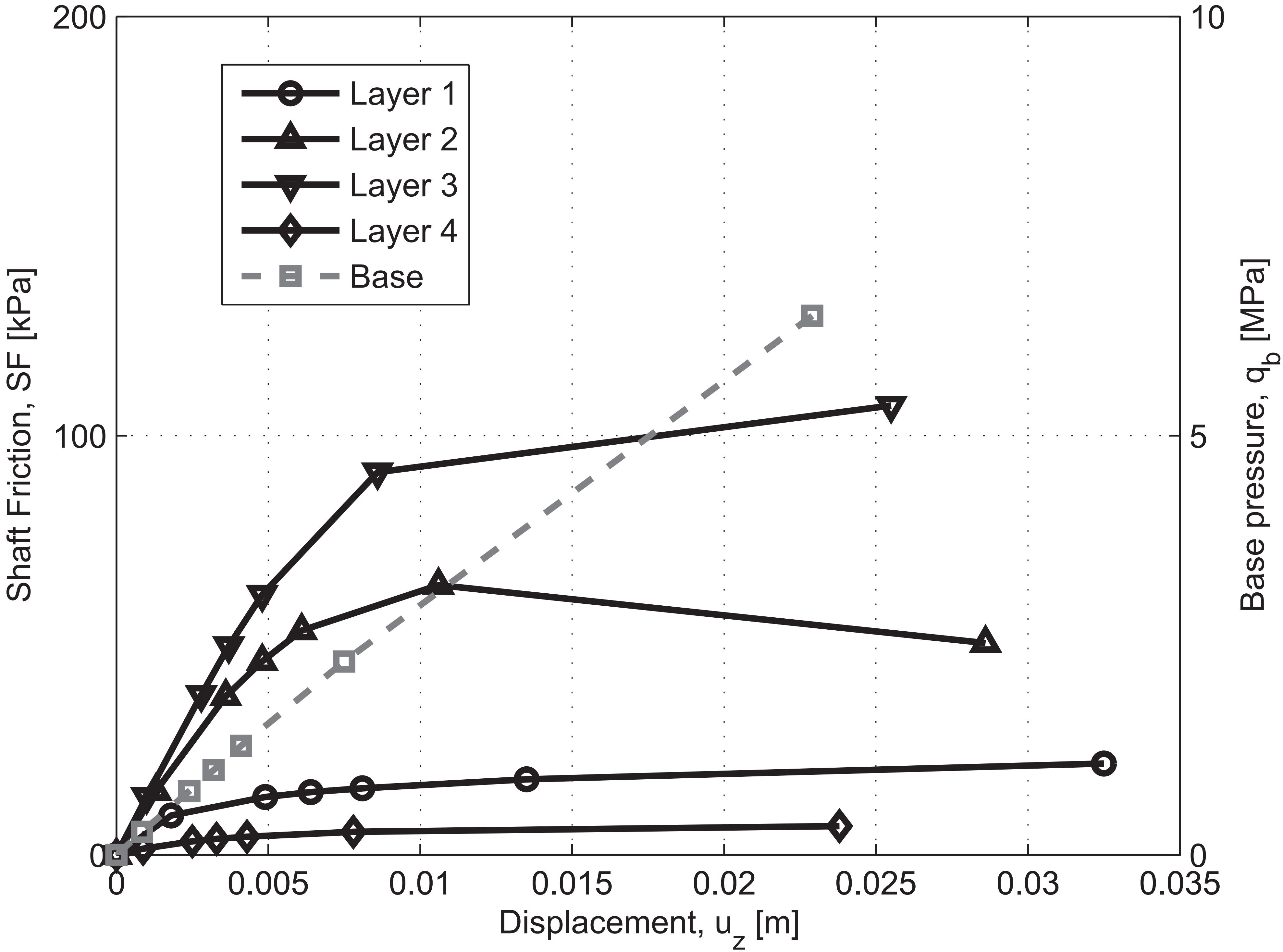

Layer 1
Layer 2
Layer 3
Layer 4
Base
Shaft Friction, SF [kPa]
Base pressure, q_b [MPa]
Displacement, u_z [m]
200
100
0
10
5
0
0
0.005
0.01
0.015
0.02
0.025
0.03
0.035

Click here to download Figure Fig_07d.eps

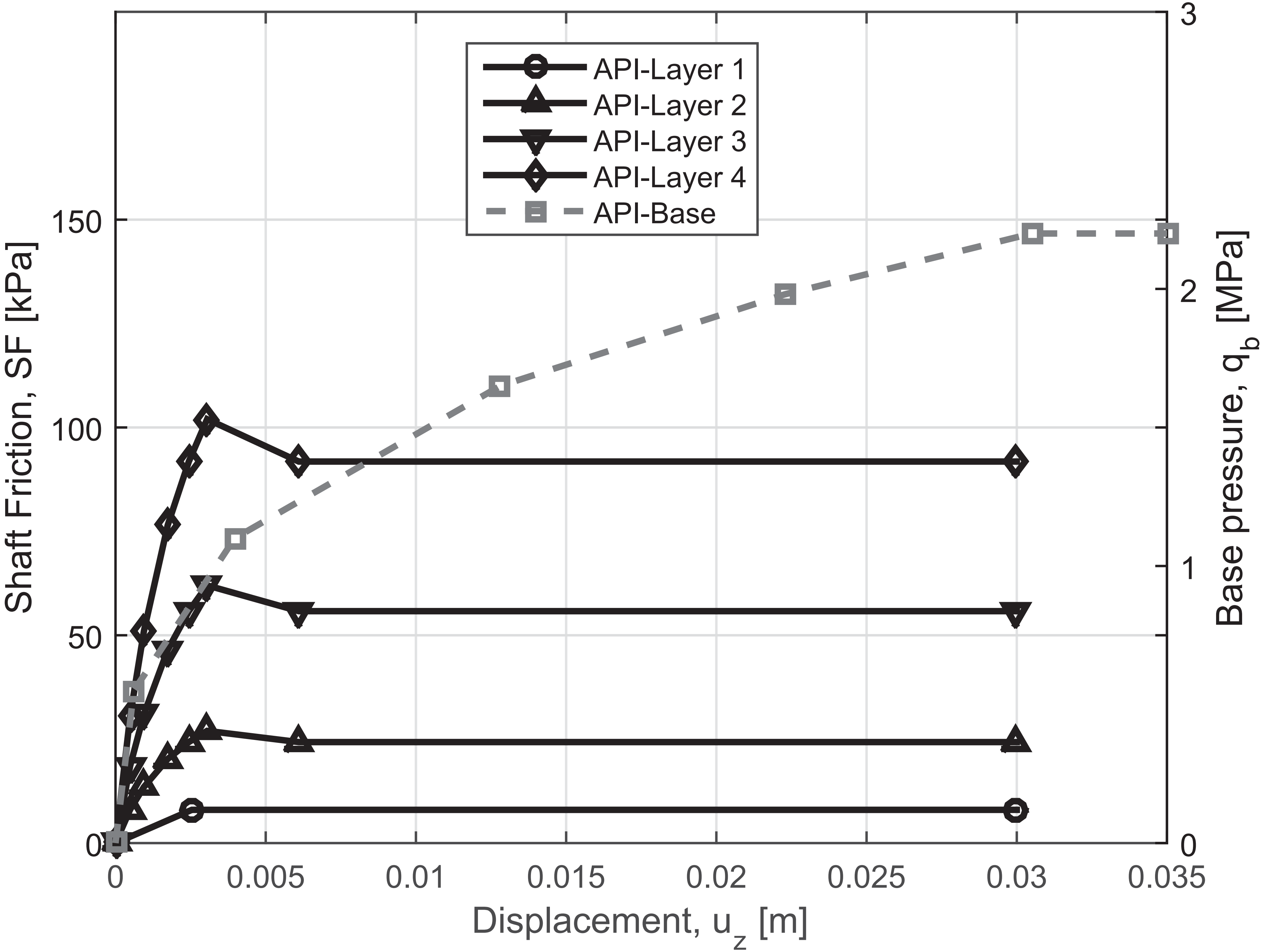

Click here to download Figure Fig_08a.eps

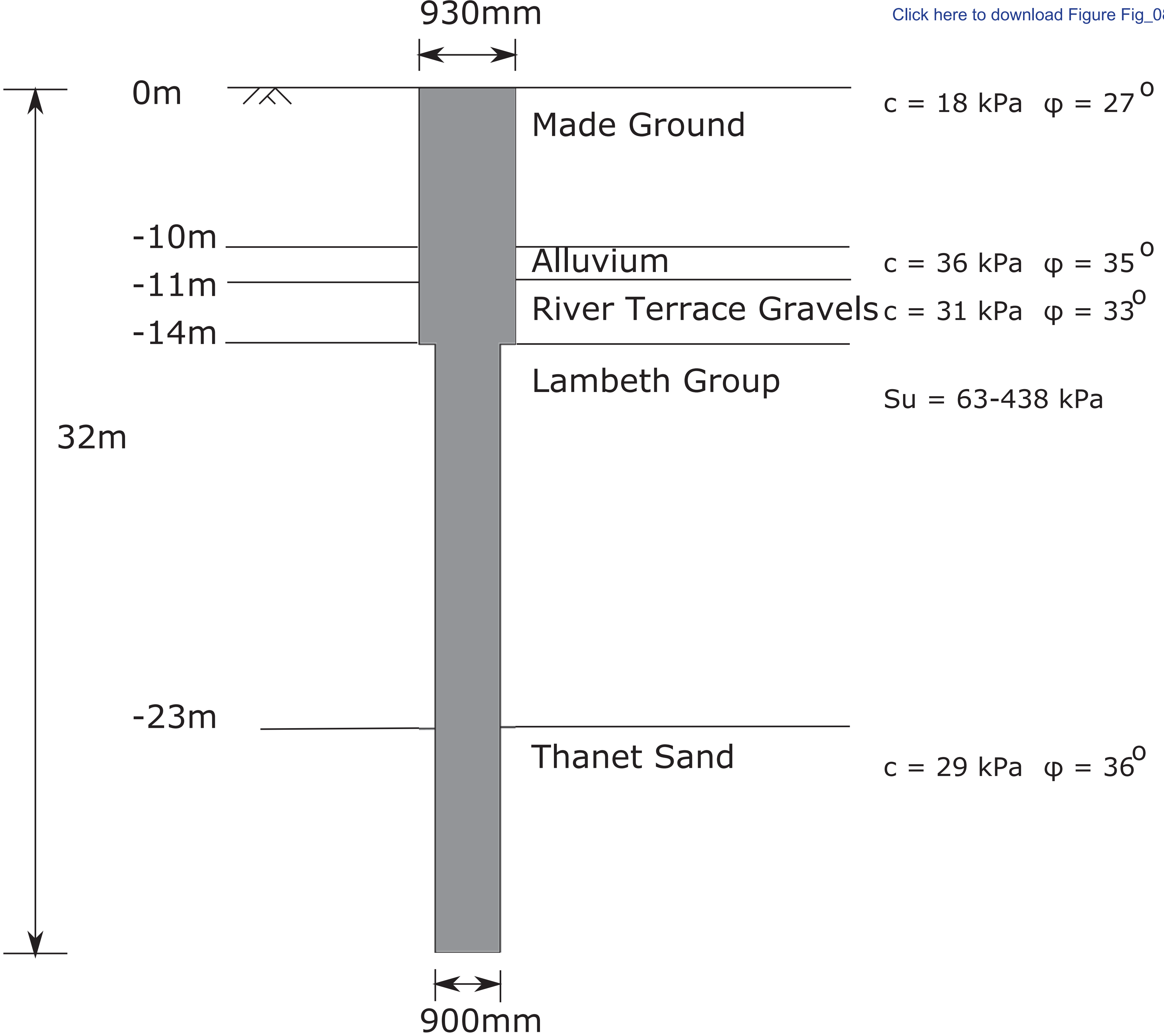

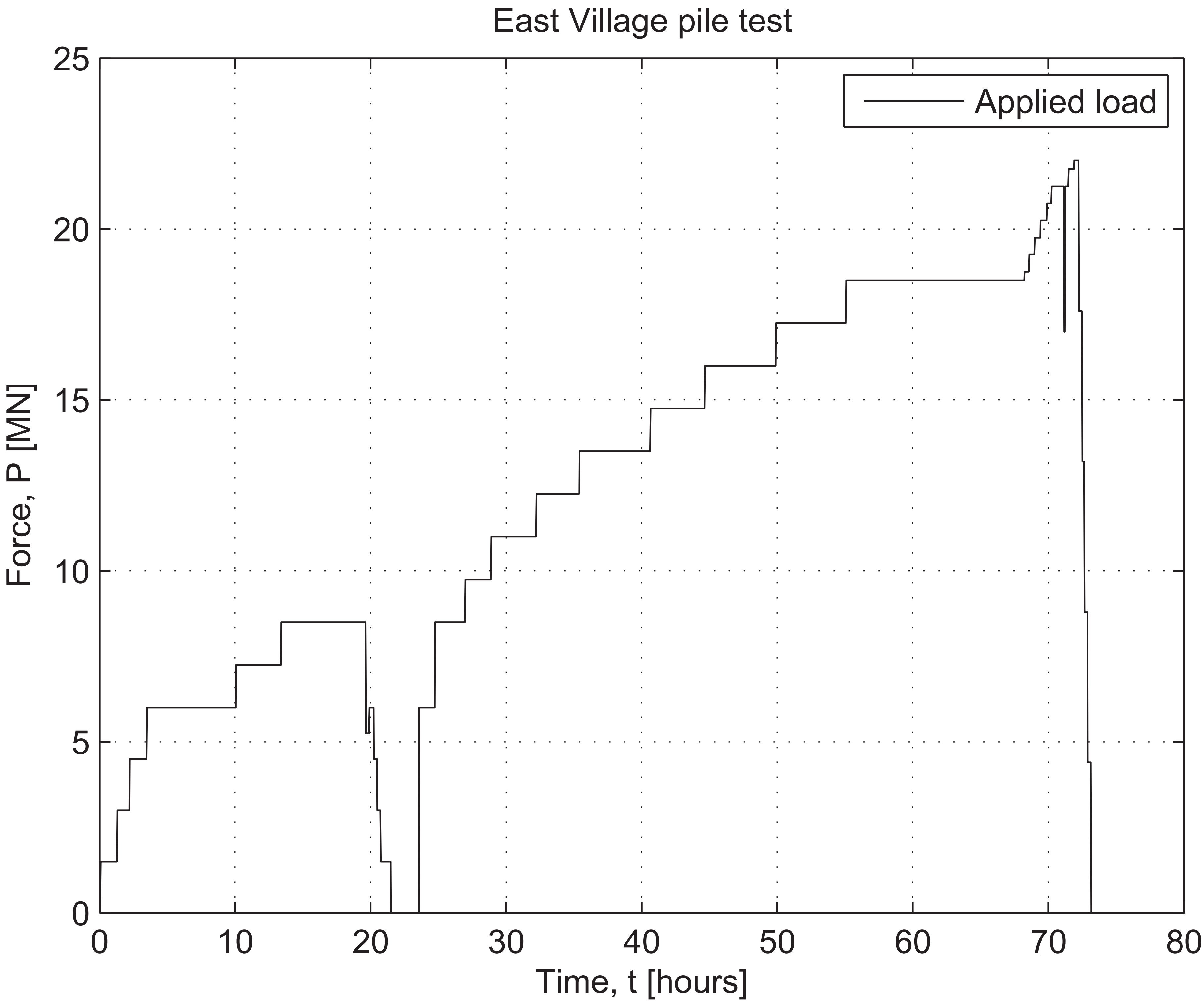

East Village pile test
Applied load
Force, P [MN]
Time, t [hours]
0
5
10
15
20
25
0
10
20
30
40
50
60
70
80

Click here to download Figure Fig_09a.eps

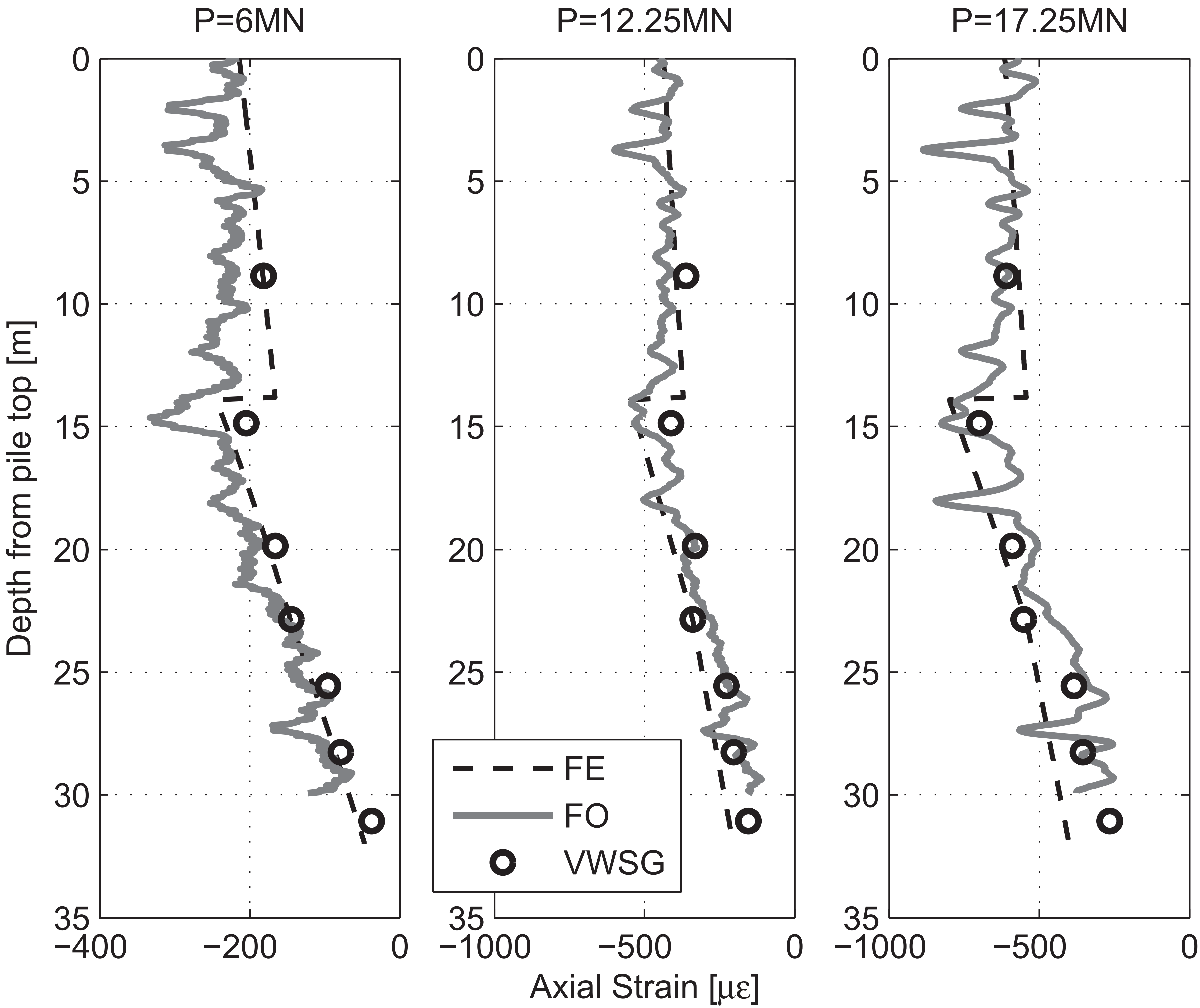

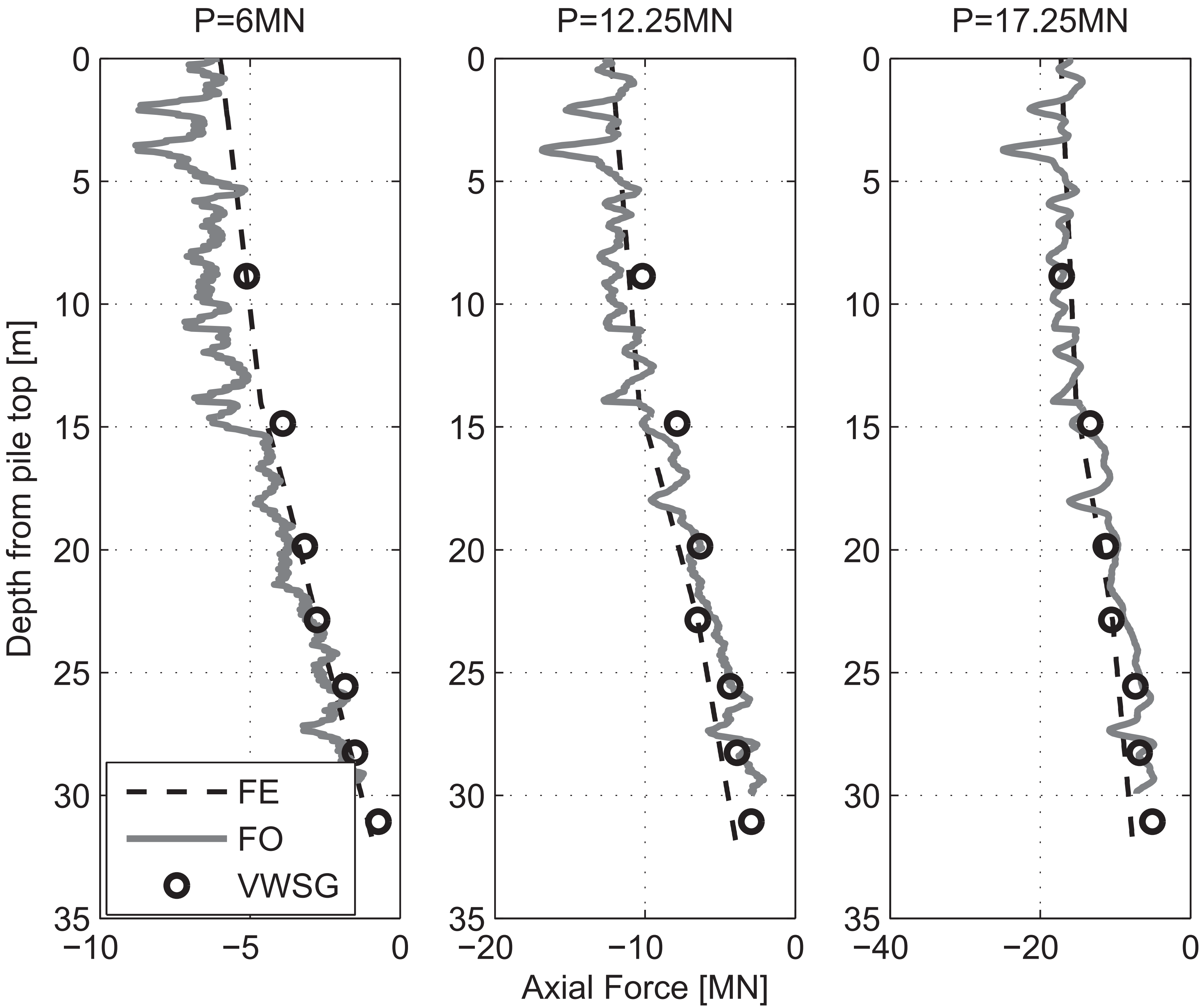
P=6MN
P=12.25MN
P=17.25MN
Depth from pile top [m]
Axial Force [MN]
FE
FO
VWSG
0
5
10
15
20
25
30
35
−10
−5
0
−20
−10
0
−40
−20
0

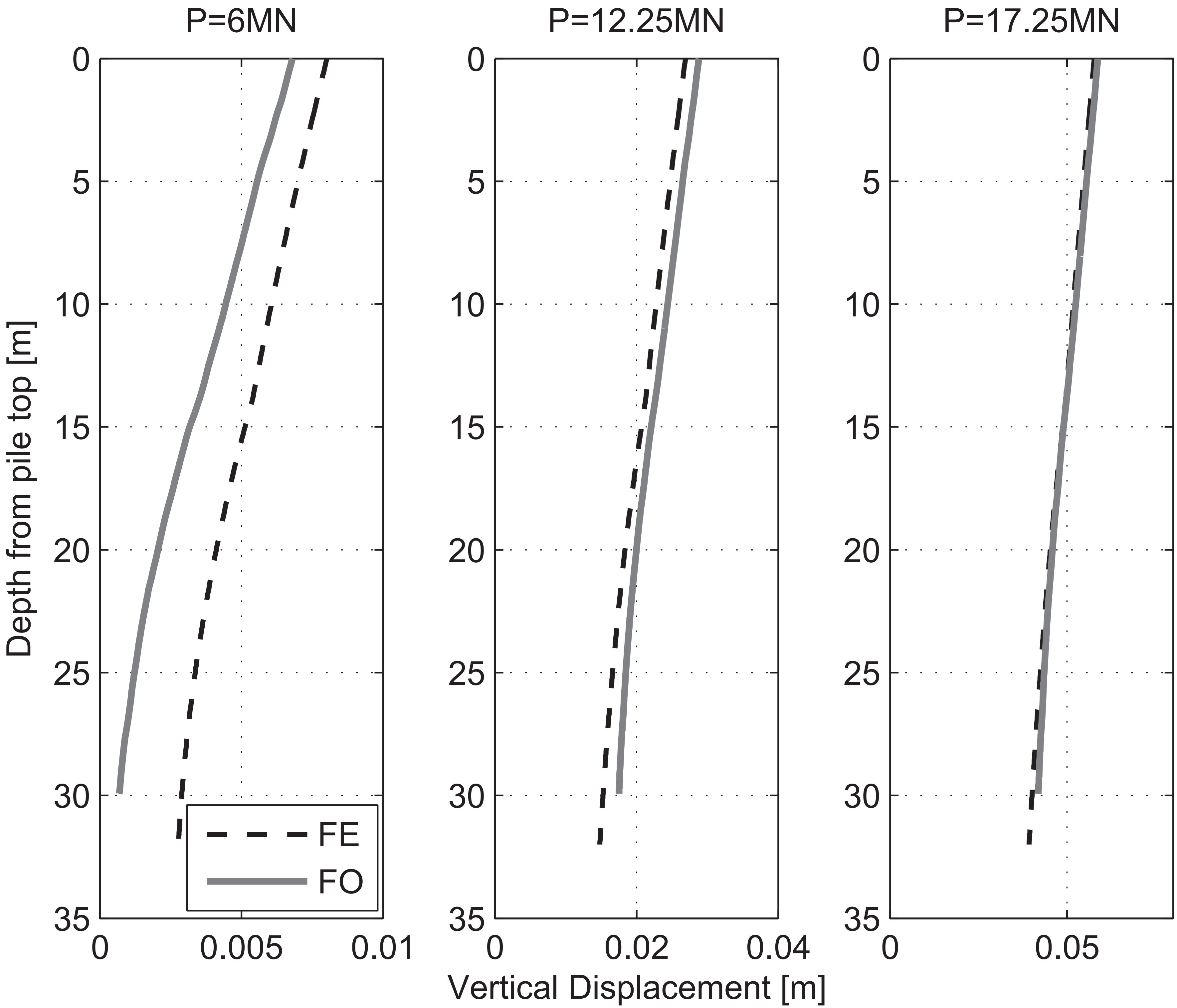
P=6MN
P=12.25MN
P=17.25MN
0
5
10
15
20
25
30
35
Depth from pile top [m]
0
0.005
0.01
0.02
0.04
0.05
Vertical Displacement [m]
FE
FO

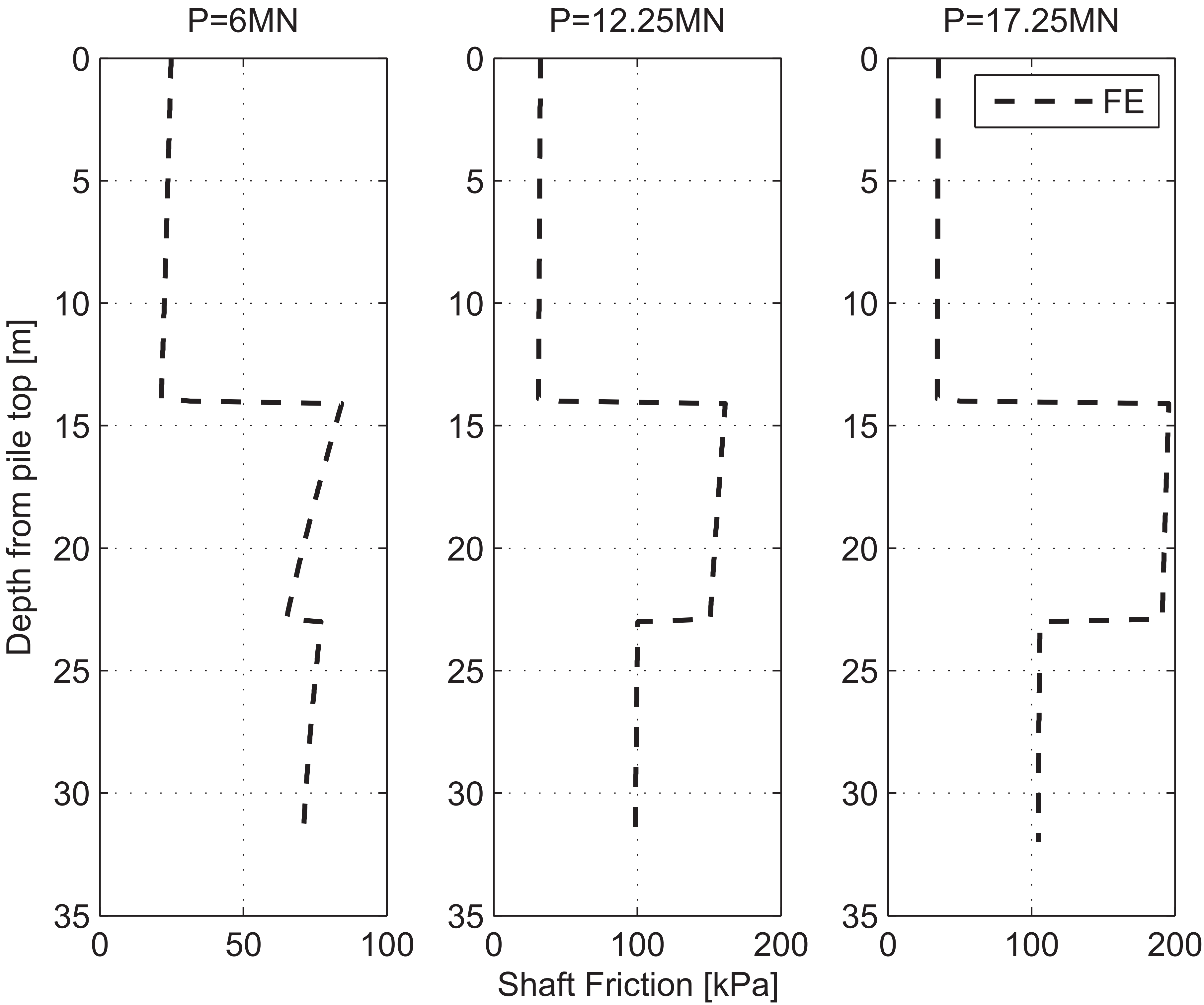
P=6MN
P=12.25MN
P=17.25MN
FE
Depth from pile top [m]
Shaft Friction [kPa]
0
5
10
15
20
25
30
35
0
50
100
0
100
200
0
100
200

Click here to download Figure Fig_10b.eps

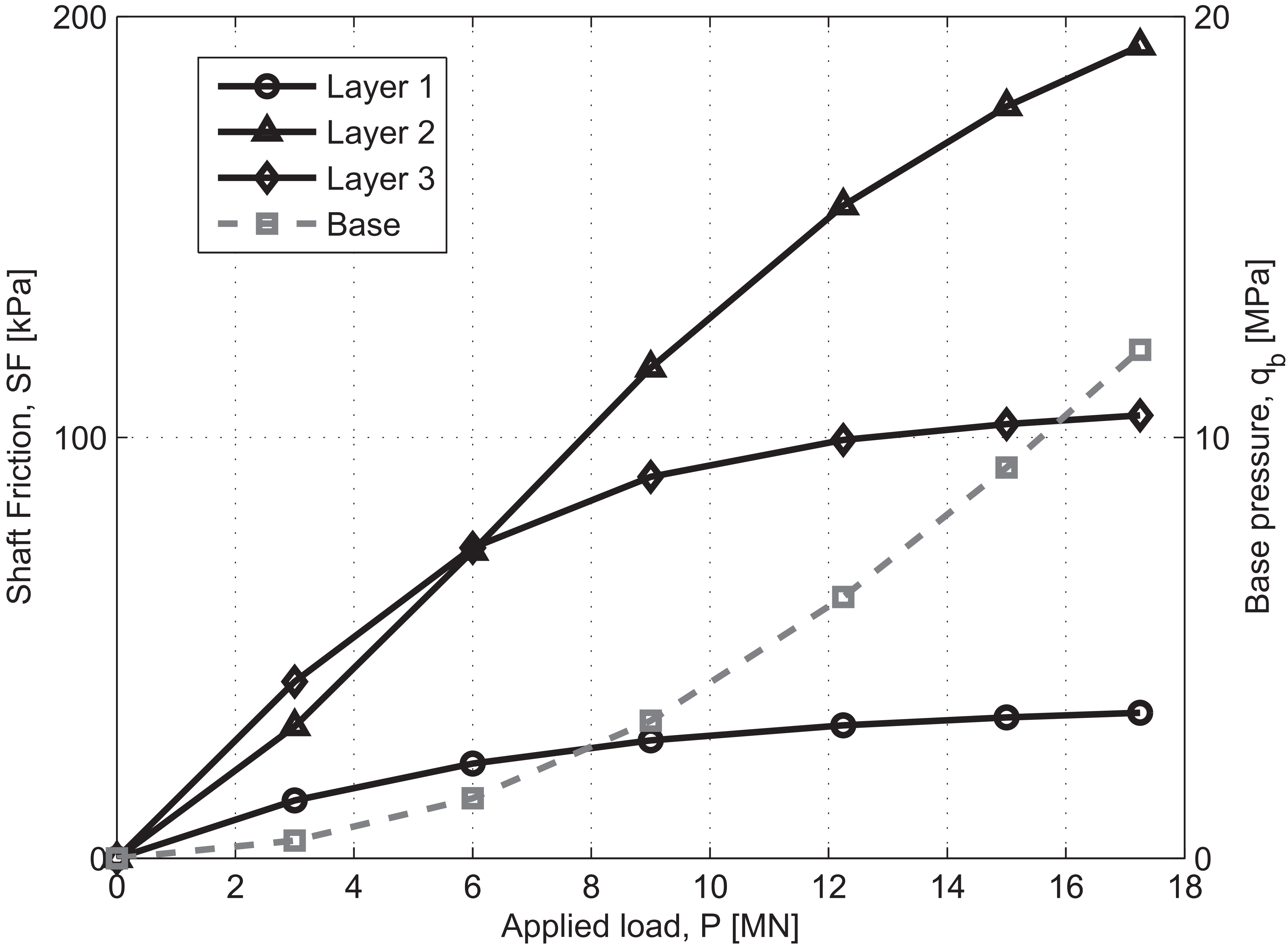

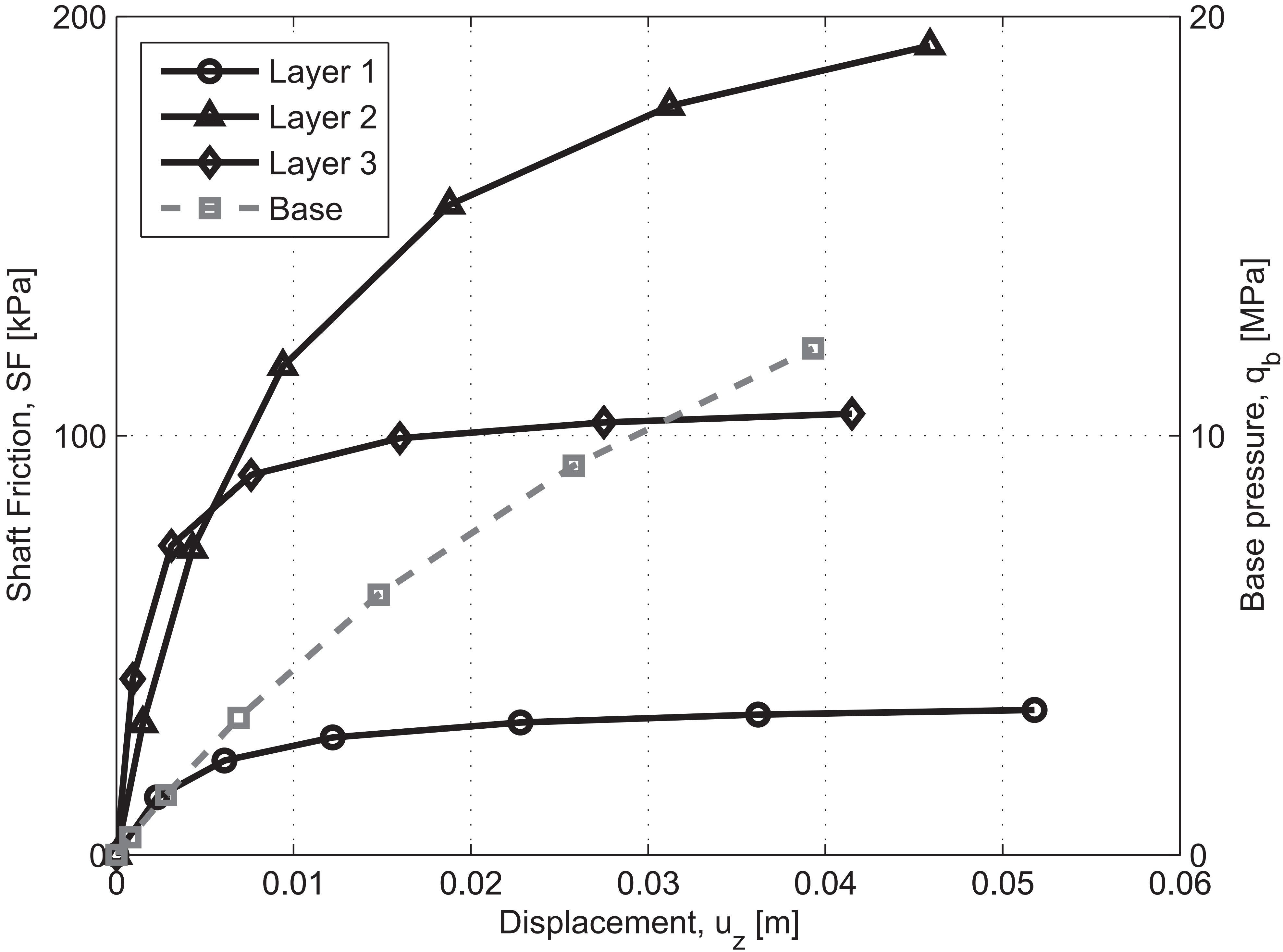

Layer 1
Layer 2
Layer 3
Base
Shaft Friction, SF [kPa]
Base pressure, q_b [MPa]
Displacement, u_z [m]
0
100
200
0
10
20
0
0.01
0.02
0.03
0.04
0.05
0.06

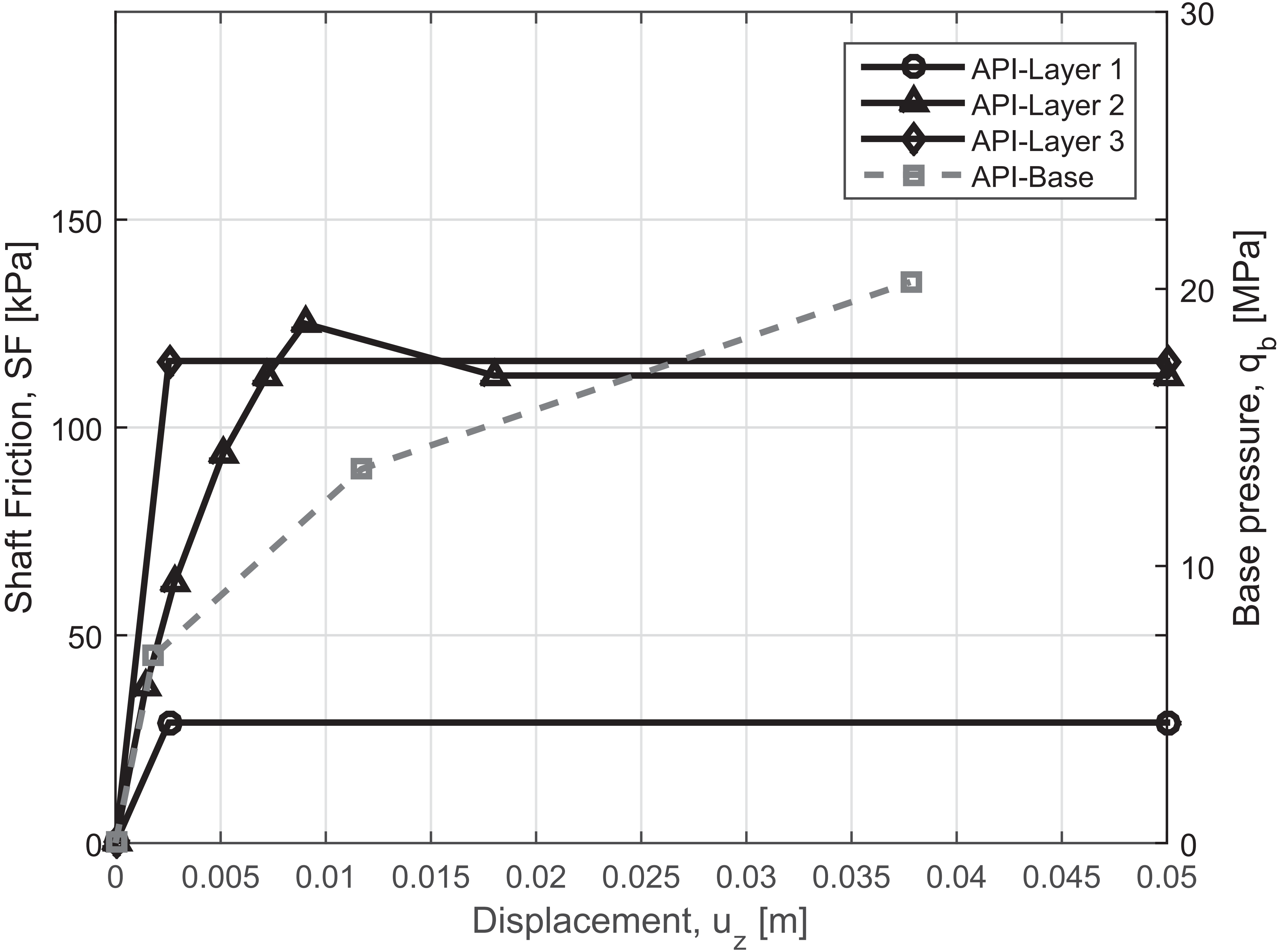

API-Layer 1
API-Layer 2
API-Layer 3
API-Base
Shaft Friction, SF [kPa]
Base pressure, q_b [MPa]
Displacement, u_z [m]
0
50
100
150
0
10
20
30
0
0.005
0.01
0.015
0.02
0.025
0.03
0.035
0.04
0.045
0.05

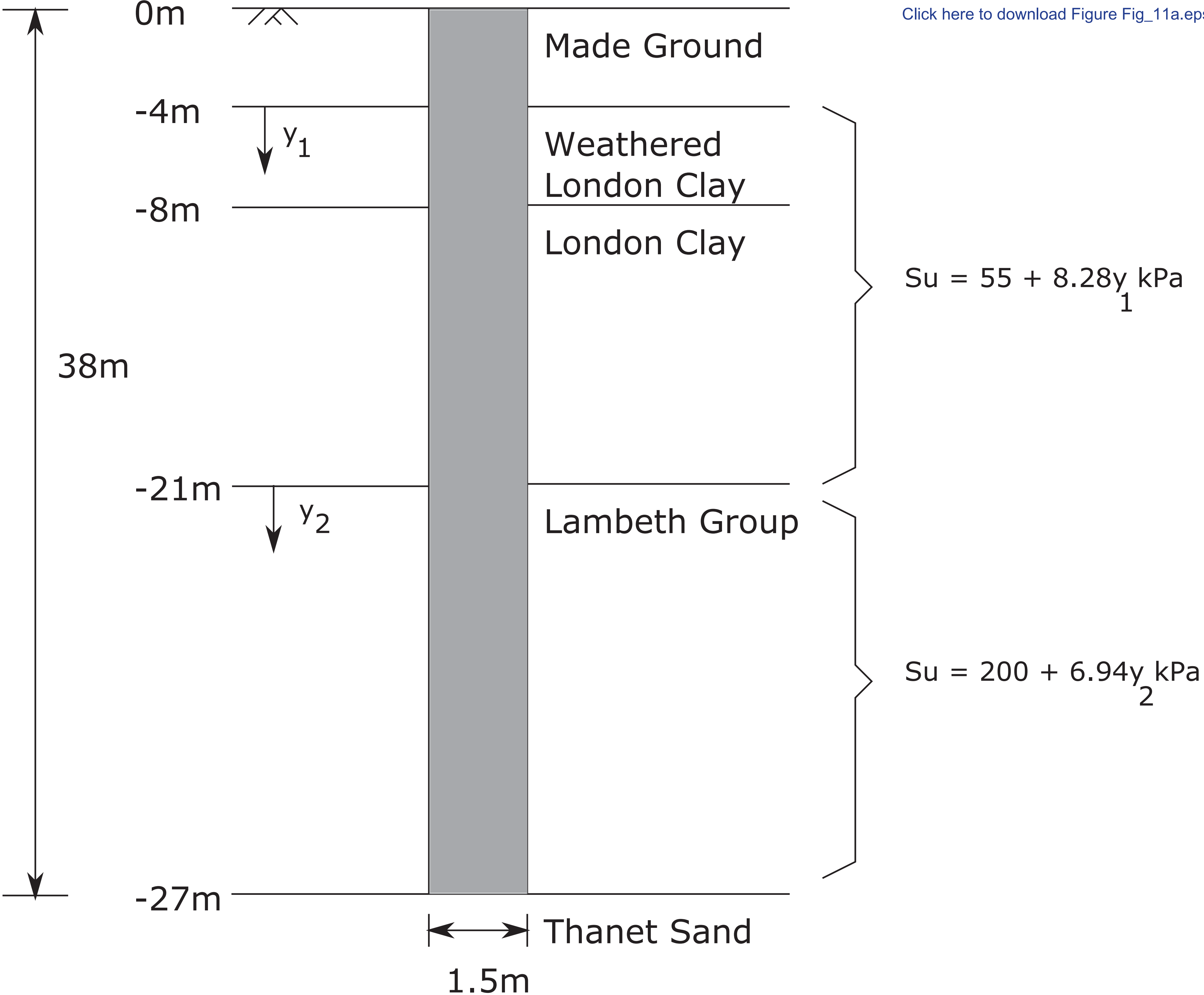
0m
-4m
-8m
-21m
-27m
38m
y_1
y_2
Made Ground
Weathered London Clay
London Clay
Lambeth Group
Thanet Sand
1.5m
$S_u = 55 + 8.28y_1$ kPa
$S_u = 200 + 6.94y_2$ kPa

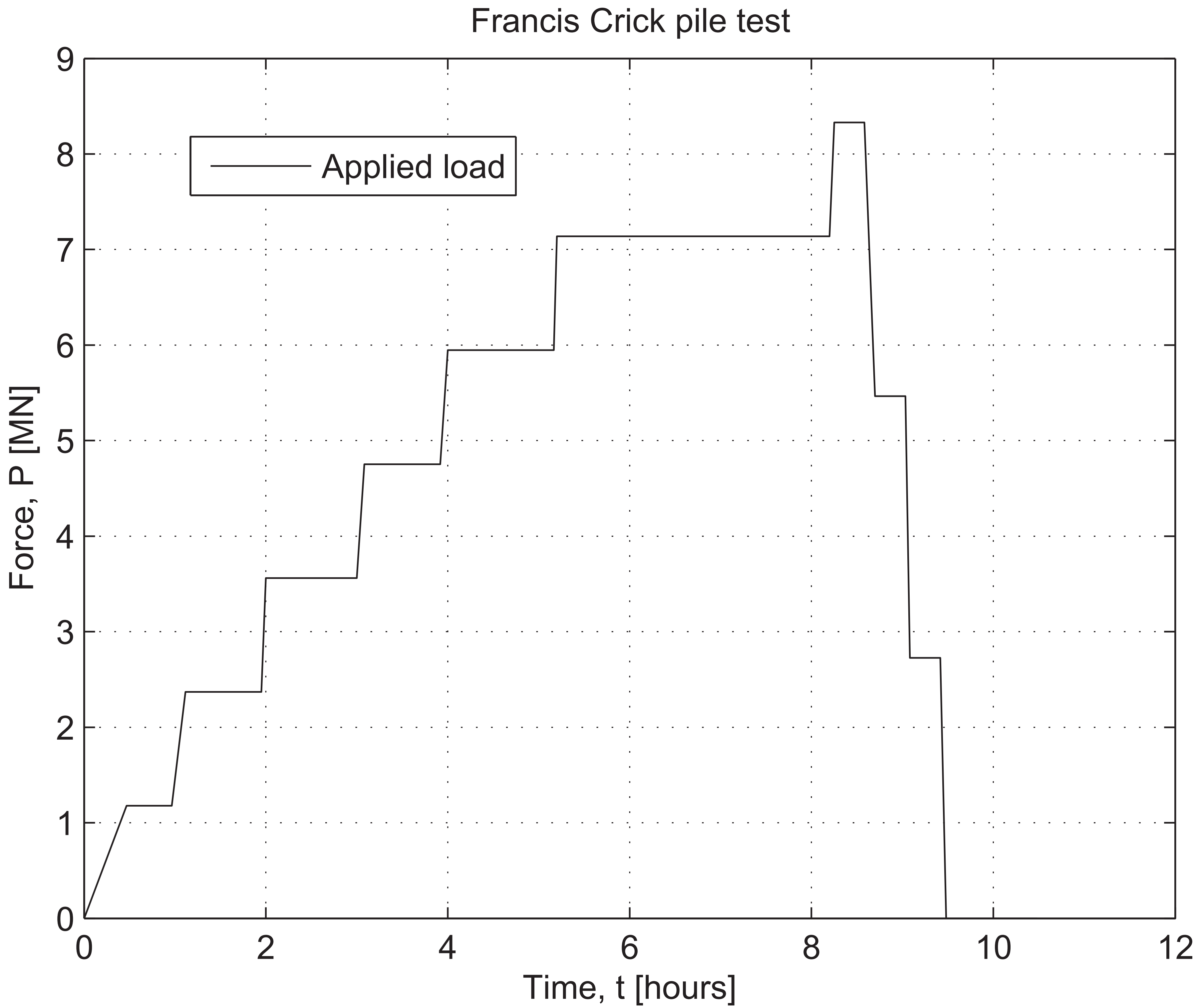
Francis Crick pile test
Applied load
Force, P [MN]
Time, t [hours]
0
1
2
3
4
5
6
7
8
9
0
2
4
6
8
10
12

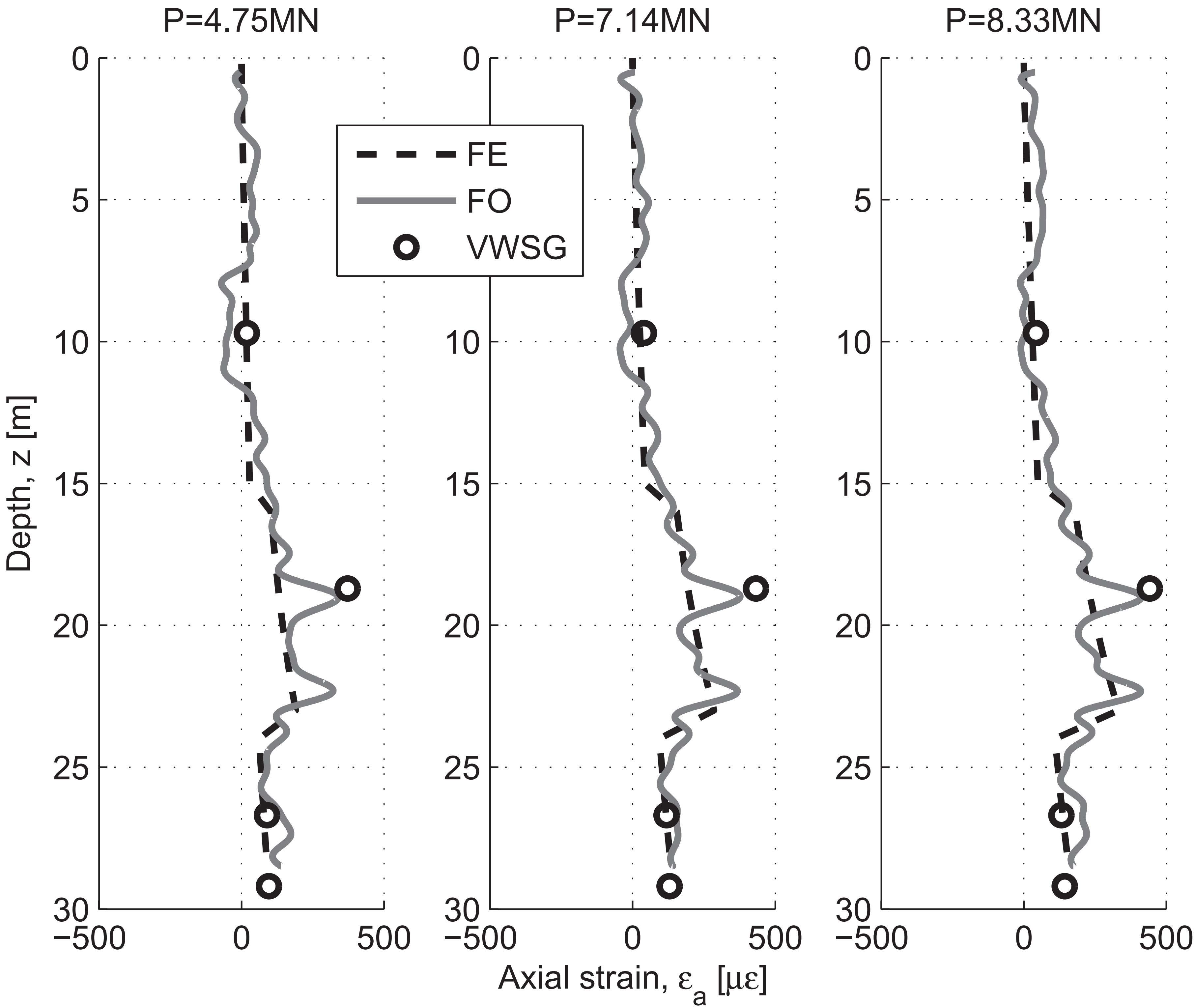
P=4.75MN
P=7.14MN
P=8.33MN
FE
FO
VWSG
Depth, z [m]
Axial strain, εa [με]
0
5
10
15
20
25
30
−500
0
500

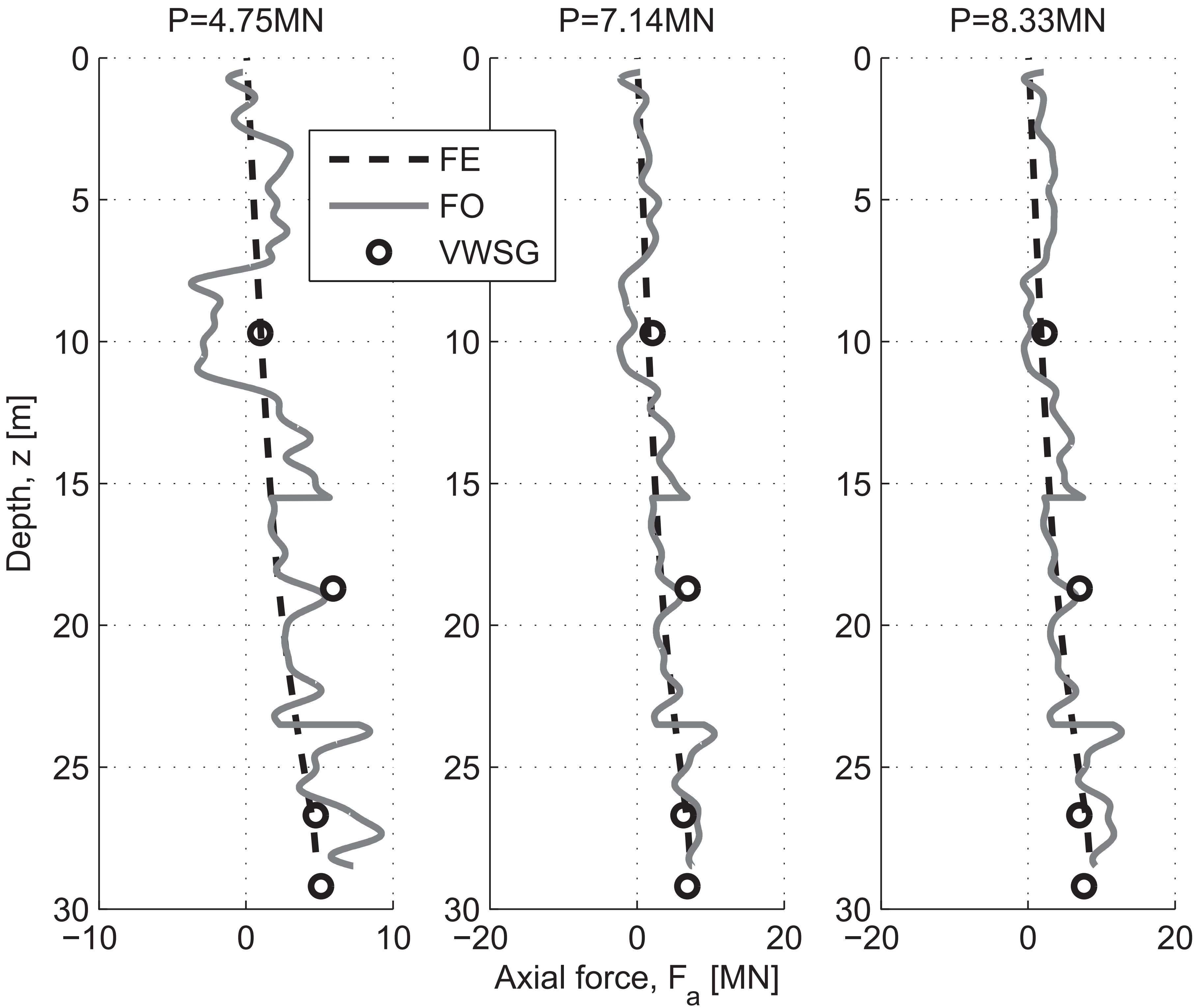
P=4.75MN
P=7.14MN
P=8.33MN
FE
FO
VWSG
Depth, z [m]
Axial force, F_a [MN]
0
5
10
15
20
25
30
−10
0
10
−20
0
20
−20
0
20

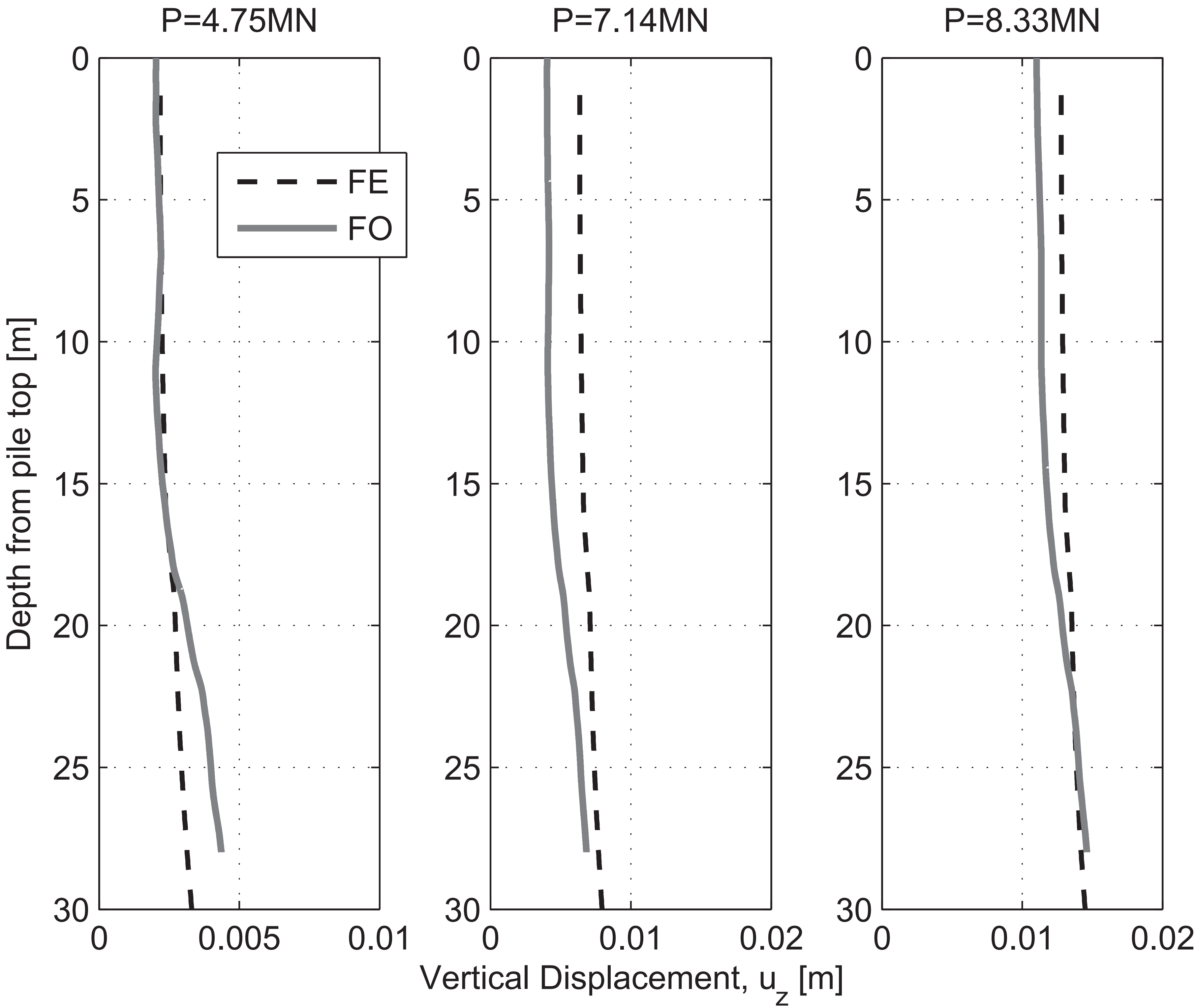
P=4.75MN
P=7.14MN
P=8.33MN
FE
FO
Depth from pile top [m]
0
5
10
15
20
25
30
0
0.005
0.01
0.02
Vertical Displacement, u_z [m]

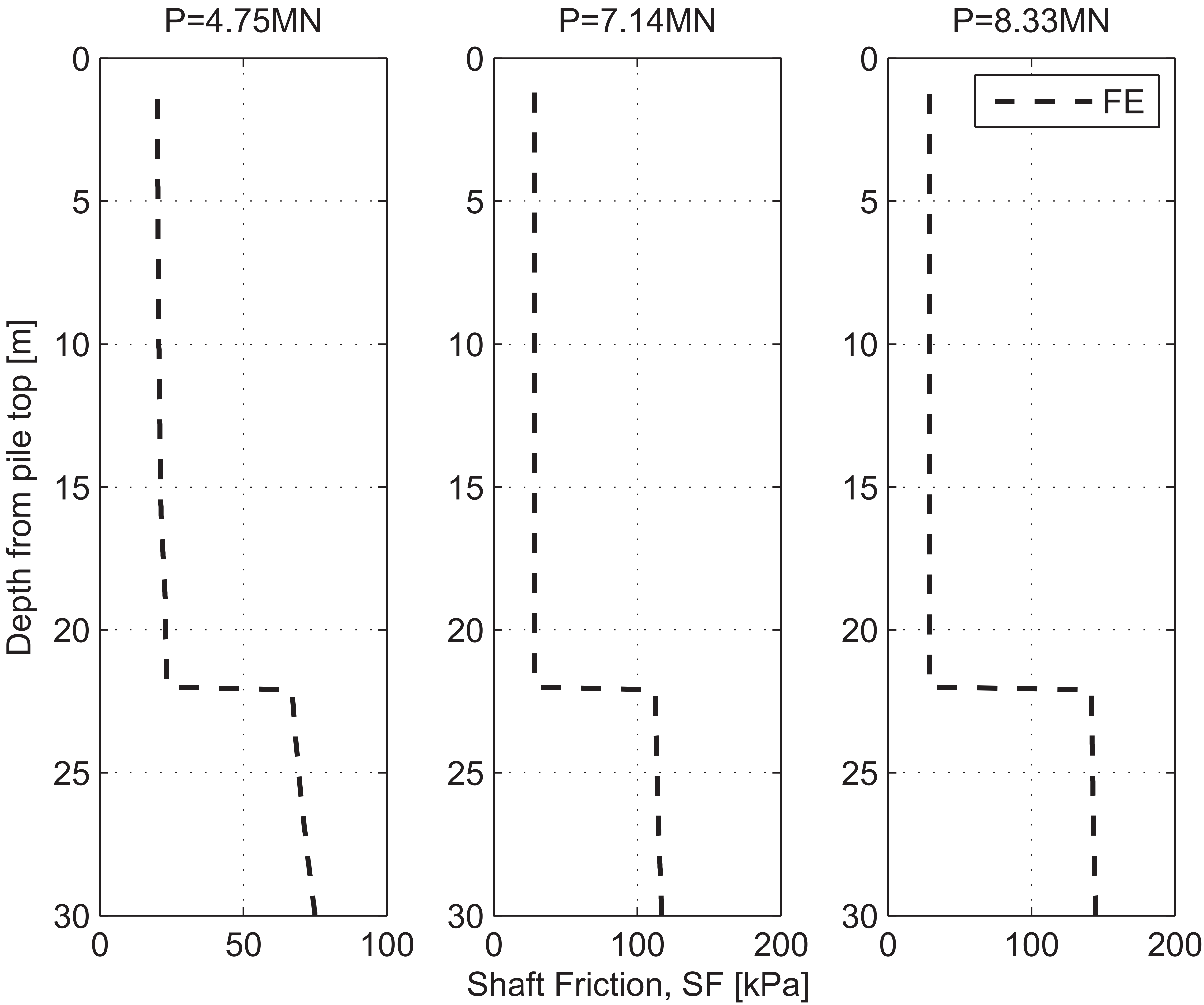
P=4.75MN
P=7.14MN
P=8.33MN
FE
Depth from pile top [m]
0
5
10
15
20
25
30
0
50
100
0
100
200
0
100
200
Shaft Friction, SF [kPa]

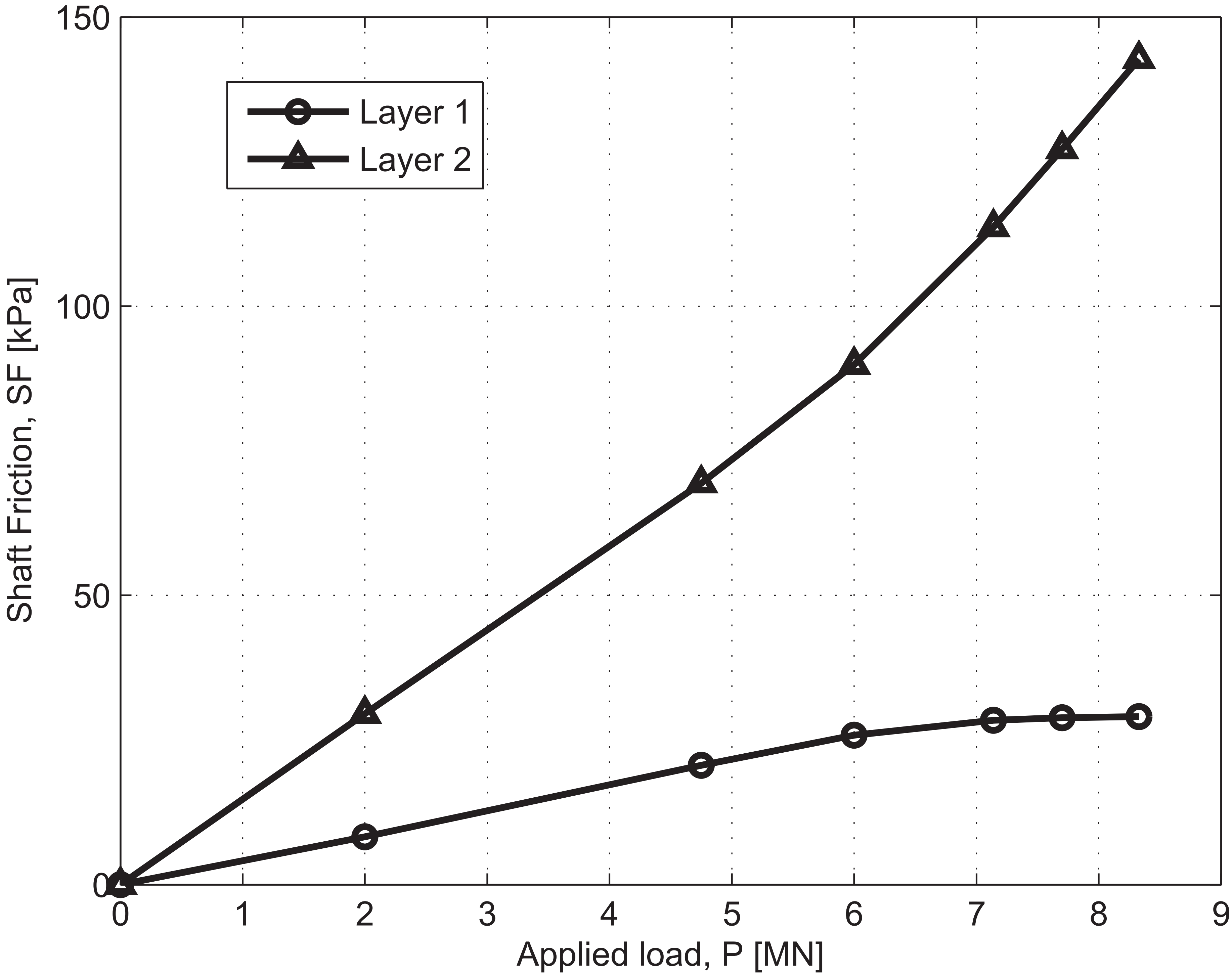

Layer 1
Layer 2
Shaft Friction, SF [kPa]
Applied load, P [MN]
0
50
100
150
0
1
2
3
4
5
6
7
8
9

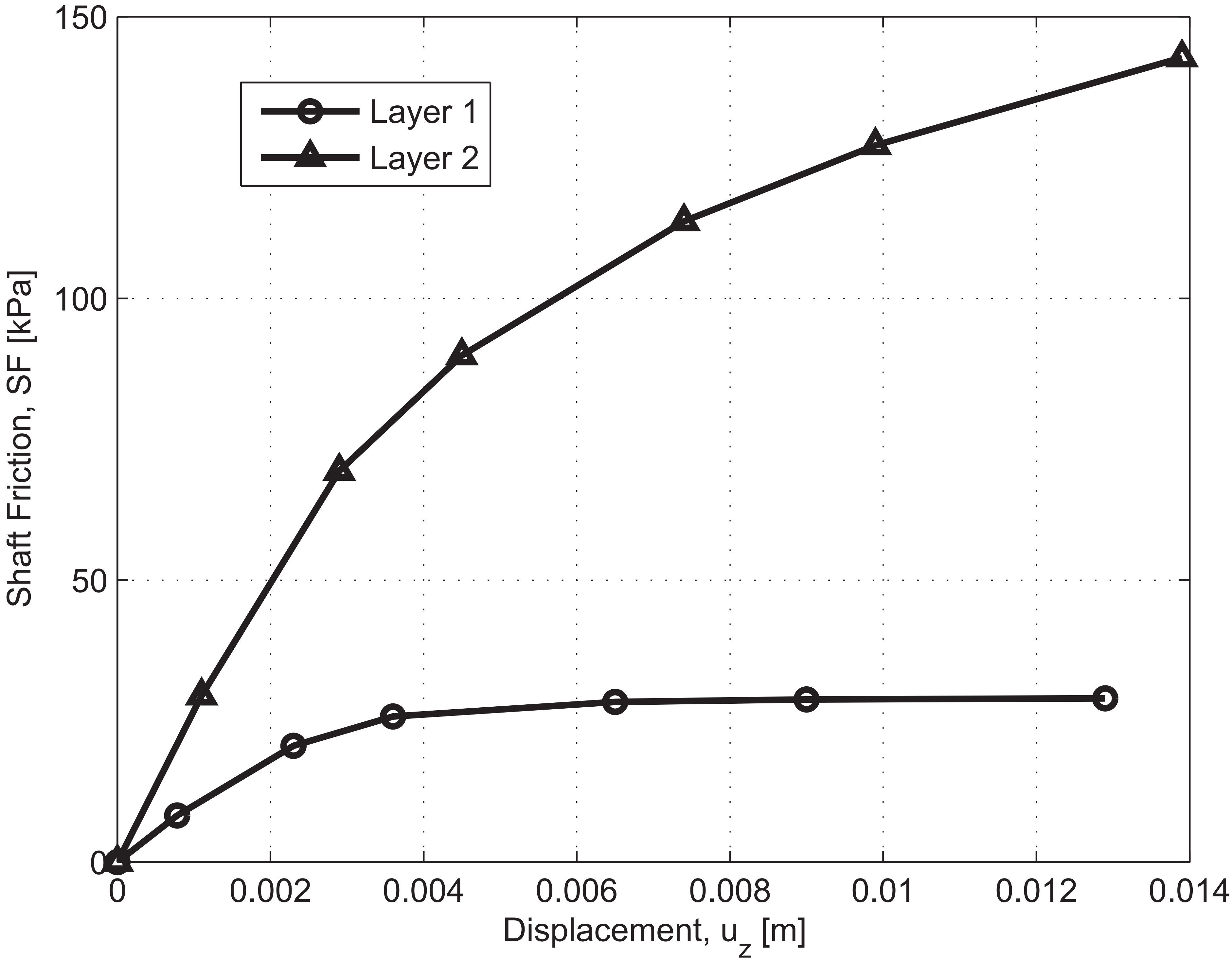

Layer 1
Layer 2
Shaft Friction, SF [kPa]
Displacement, u_z [m]
0
50
100
150
0
0.002
0.004
0.006
0.008
0.01
0.012
0.014

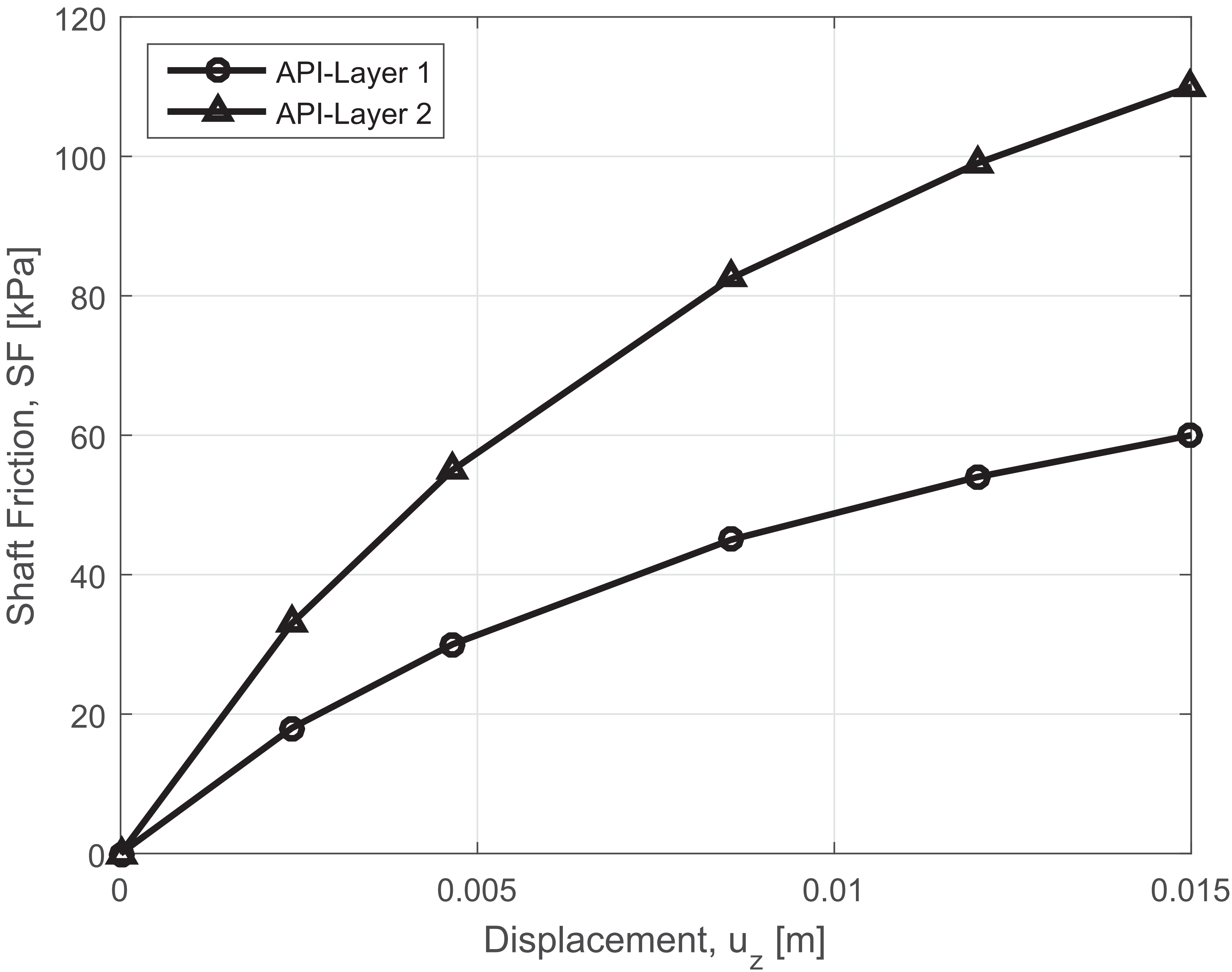

API-Layer 1
API-Layer 2
Shaft Friction, SF [kPa]
Displacement, u_z [m]
0
20
40
60
80
100
120
0
0.005
0.01
0.015

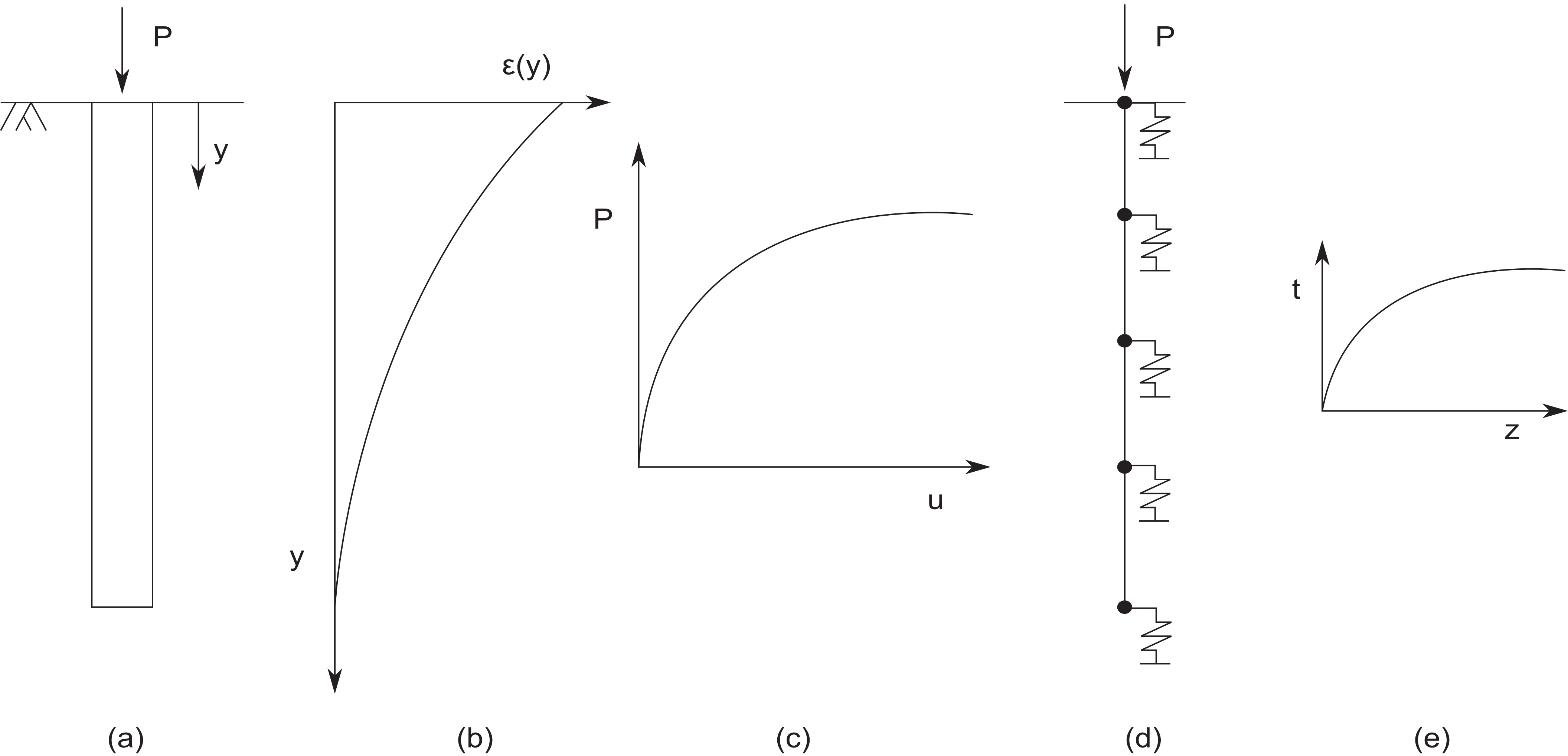

P
y
ε(y)
y
P
u
P
t
z
(a)
(b)
(c)
(d)
(e)